

FINE-SCALE STRUCTURE OF THE QUASAR 3C 279 MEASURED WITH 1.3 mm VERY LONG BASELINE INTERFEROMETRY

Ru-Sen Lu ¹, Vincent L. Fish¹, Kazunori Akiyama^{2,3}, Sheperd S. Doeleman^{1,4}, Juan C. Algaba⁵,
Geoffrey C. Bower⁶, Christiaan Brinkerink⁷, Richard Chamberlin⁸, Geoffrey Crew¹, Roger J.
Cappallo¹, Matt Dexter⁶, Robert Freund⁹, Per Friberg¹⁰, Mark A. Gurwell⁴, Paul T. P. Ho⁵,
Mareki Honma^{2,11}, Makoto Inoue⁵, Svetlana G. Jorstad^{12,13}, Thomas P. Krichbaum¹⁴, Laurent
Loinard¹⁵, David MacMahon⁶, Daniel P. Marrone⁹, Alan P. Marscher¹², James M. Moran⁴,
Richard Plambeck⁶, Nicolas Pradel⁵, Rurik Primiani⁴, Remo P. J. Tilanus^{10,16}, Michael Titus¹,
Jonathan Weintroub⁴, Melvyn Wright⁶, Ken H. Young⁴, Lucy M. Ziurys⁹

rslu@haystack.mit.edu

¹Massachusetts Institute of Technology, Haystack Observatory, Route 40, Westford, MA 01886, USA

²National Astronomical Observatory of Japan, Osawa 2-21-1, Mitaka, Tokyo 181-8588, Japan

³Department of Astronomy, Graduate School of Science, The University of Tokyo, 7-3-1 Hongo, Bunkyo-ku, Tokyo 113-0033, Japan

⁴Harvard-Smithsonian Center for Astrophysics, 60 Garden St., Cambridge, MA 02138, USA

⁵Institute of Astronomy and Astrophysics, Academia Sinica, P.O. Box 23-141, Taipei 10617, Taiwan, R.O.C.

⁶University of California Berkeley, Dept. of Astronomy, Radio Astronomy Laboratory, 601 Campbell, Berkeley, CA 94720-3411, USA

⁷Department of Astrophysics, IMAPP, Radboud University Nijmegen, P.O. Box 9010, 6500 GL Nijmegen, The Netherlands

⁸Caltech Submillimeter Observatory, 111 Nowelo Street, Hilo, HI 96720, USA

⁹Arizona Radio Observatory, Steward Observatory, University of Arizona, 933 North Cherry Ave., Tucson, AZ 85721-0065, USA

¹⁰James Clerk Maxwell Telescope, Joint Astronomy Centre, 660 North A'ohoku Place, University Park, Hilo, HI 96720, USA

¹¹The Graduate University for Advanced Studies, Osawa 2-21-1, Mitaka, Tokyo, 181-8588, Japan

¹²Institute for Astrophysical Research, Boston University, Boston, MA 02215

¹³Astronomical Institute, St. Petersburg State University, Universitetskij Pr. 28, Petrodvorets, 198504 St. Petersburg, Russia

¹⁴Max-Planck-Institut für Radioastronomie, Auf dem Hügel 69, D-53121 Bonn, Germany

¹⁵Centro de Radioastronomía y Astrofísica, Universidad Nacional Autónoma de México, 58089 Morelia, Michoacán, México

¹⁶Netherlands Organization for Scientific Research, Laan van Nieuw Oost-Indie 300, NL2509 AC The Hague, The Netherlands

ABSTRACT

We report results from 5-day VLBI observations of the well-known quasar 3C 279 at 1.3 mm (230 GHz) in 2011. The measured nonzero closure phases on triangles including stations in Arizona, California and Hawaii indicate that the source structure is spatially resolved. We find an unusual inner jet direction at scales of ~ 1 parsec extending along the northwest-southeast direction ($PA = 127^\circ \pm 3^\circ$), as opposed to other (previously) reported measurements on scales of a few parsecs showing inner jet direction extending to the southwest. The 1.3 mm structure corresponds closely with that observed in the central region of quasi-simultaneous super-resolution VLBA images at 7 mm. The closure phase changed significantly on the last day when compared with the rest of observations, indicating that the inner jet structure may be variable on daily timescales. The observed new direction of the inner jet shows inconsistency with the prediction of a class of jet precession models. Our observations indicate a brightness temperature of $\sim 8 \times 10^{10}$ K in the 1.3 mm core, much lower than that at centimeter wavelengths. Observations with better uv coverage and sensitivity in the coming years will allow the discrimination between different structure models and will provide direct images of the inner regions of the jet with 20–30 μas (5–7 light months) resolution.

Subject headings: Galaxies: active - galaxies: jets - quasars: individual (3C 279) - radio continuum: galaxies

1. Introduction

Highly beamed relativistic jets associated with active galactic nuclei (AGN) are believed to be powered by accretion of the central super massive black holes and/or their spin. The creation mechanism of these jets, however, remains an enigma. VLBI observations at short millimeter wavelengths provide the highest angular resolution achievable in astronomy and allow us to explore the compact core regions of these jets, which are self-absorbed at longer wavelengths. In recent years, VLBI observations at 3.5 mm have been regularly performed either with the Global Millimeter VLBI array (GMVA) or with the standalone Very Long Baseline Array (VLBA). At 1.3 mm, significant progress has been achieved in the last few years with the Event Horizon Telescope (EHT) (Sgr A*: [Doeleman et al. 2008](#), [Fish et al. 2011](#), 1921-293: [Lu et al. 2012](#), M87: [Doeleman et al. 2012](#)).

At a redshift of $z = 0.536$ (Marziani et al. 1996), the quasar 3C 279 (B1253-055, 1 mas corresponding to 6.31 pc and 0.1 mas/yr corresponding to a transverse velocity of $3.2c$, assuming a standard cosmological model with $H_0 = 71 \text{ km s}^{-1} \text{ Mpc}^{-1}$, $\Omega_M = 0.27$, $\Omega_\Lambda = 0.73$) is one of the brightest radio sources. It is the first source in which superluminal motion was discovered (Whitney et al. 1971), with its jet oriented very close to the line of sight ($0.1^\circ - 5.0^\circ$, Bloom et al. 2013). The high brightness and compactness made 3C 279 one of the primary targets for high-frequency VLBI fringe detections (Greve et al. 2002; Krichbaum et al. 1997). It is known for its rapid variations across the entire electromagnetic spectrum with various timescales from hours/days to years, and has been monitored intensively at various wavelengths (e.g., Larionov et al. 2008; Collmar et al. 2010; Hayashida et al. 2012).

The large-scale radio structure of 3C 279 is characterized by a compact flat-spectrum core with a jet extending to about $5''$ along a position angle of 205° (measured north through east) and a radio lobe extending to the northwest about $10''$ away (e.g., de Pater & Perley 1983). Cheung (2002) detected optical and ultraviolet emission from the kiloparsec-scale jet and found a bright knot coincident with a peak in the radio jet $\sim 0.6''$ from the nucleus.

3C 279 has been closely monitored with VLBI over 4 decades, yielding a wealth of detailed information about the jet on parsec scales (e.g., Cohen et al. 1971; Cotton et al. 1979; Pauliny-Toth et al. 1981; Unwin et al. 1989; Jorstad et al. 2001; Wehrle et al. 2001; Homan et al. 2003; Jorstad et al. 2005; Chatterjee et al. 2008). On VLBI scales, the structure is dominated by a jet extending to the southwest, with multiple projected apparent speeds and position angles. Polarimetric observations have detected both linearly and circularly polarized emission from the parsec-scale jet of 3C 279 (e.g., Leppänen et al. 1995; Wardle et al. 1998; Taylor 2000; Attridge 2001; Zavala & Taylor 2001; Homan et al. 2009). The first detection of circular polarization has been used to argue for an electron-positron composition of the jet (Wardle et al. 1998).

In this paper we present results from high-resolution 1.3 mm VLBI observations of 3C 279. Section 2–3 summarizes the EHT observations at 1.3 mm, data reduction, and calibration. § 4 describes the results from these observations, and the source structure at 7 mm from VLBA observations, followed by discussion in § 5. § 6 summarizes our conclusions.

2. Observations

An ensemble of sources (3C 273, M 87, 3C 279, 1633+382, 3C 345, NRAO 530, Sgr A*, 1749+096, 1921-293, BL Lac, 3C 454.3) was observed with the EHT during the nights of 2011 March 29 and 31 and 2011 April 01, 02, and 04 (days 88, 90, 91, 92, and 94). Here we focus on the source 3C 279 and others will be presented elsewhere. Left circular polarization was observed

at all sites. Two 480-MHz bandwidths were centered at 229.089 and 229.601 GHz (referred to as the low and high bands, respectively). The DBE1 digital backend designed at MIT Haystack Observatory was used for all single-antenna stations. Beamformers at the Submillimeter Array (SMA) and Combined Array for Research in Millimeter-wave Astronomy (CARMA) are based on the DBE1 architecture as well. Both the DBE1 and beamformer systems channelize the data into 15 32-MHz channels. Hydrogen masers were used as timing and frequency references at all sites, with the exception that the 10 MHz reference signal for the 1024 MHz sampler clock in the digital backends at CARMA was erroneously derived from a local rubidium oscillator instead of the hydrogen maser on days 88-92; the hydrogen maser was used on day 94. Data were recorded onto modules of hard drives using the Mark 5B+ system and correlated with the Haystack Mark 4 VLBI correlator using 32 lags and an accumulation period of 1 s.

The array consisted of seven stations located at three different sites: the CARMA site in California, Mauna Kea in Hawaii, and Mount Graham in Arizona. The stations are indicated by the one-letter codes used hereafter (Table 1):

- C** A single 10.4-m CARMA antenna (C4). The CARMA beamformer was used in a “passthrough” mode as the backend.
- D** A single 10.4-m CARMA antenna (C1) using a DBE1 backend.
- F** The phased sum of seven CARMA antennas. Signals from three 10.4-m and four 6.1-m antennas were added using the CARMA beamformer. Only the high band was phased. Station F replaced station C in the high band when it was used on days 91-94.
- J** The James Clerk Maxwell Telescope (JCMT), using a DBE1 backend. Station J was used as a standalone antenna on day 88 only.
- O** The Caltech Submillimeter Observatory (CSO), using a DBE1 backend. Station O was used as a standalone antenna on days 90–94.
- P** The phased sum of seven SMA antennas plus either the CSO (day 88) or the JCMT (days 90–94).
- S** The Arizona Radio Observatory Submillimeter Telescope (SMT) on Mount Graham.

2.1. Weather

Observations were triggered at all sites several hours before the start of each night’s schedule based on expected weather conditions. On Mauna Kea 90% of zenith opacity measurements

Table 1: Array description.

Facility	Code	Effective aperture (m)	Days	Note
CARMA	C	10.4	88–94	single dish, high band replaced by F on days 90–94
CARMA	D	10.4	88–94	single dish
CARMA	F	21.8	91–94	$3 \times 10.4\text{m} + 4 \times 6.1\text{m}$ (high band only)
Hawaii	J	15.0	88	JCMT standalone
Hawaii	O	10.4	90–94	CSO standalone
Hawaii	P	19.0/21.8	88–94	SMA ($7 \times 6.0\text{m}$) + CSO (day 88)/JCMT (days 90–94)
SMT	S	10.0	88–94	

over the course of the five nights of observations fell into the range of 0.04–0.15. The 90% opacity ranges at the SMT and CARMA were 0.11–0.34 and 0.23–0.48, respectively. Atmospheric coherence was poor at the CARMA site on day 92, with effects as noted in the following sections.

3. Data Reduction and Calibration

We reduced the data using the Haystack Observatory Postprocessing System (HOPS). Variable tropospheric conditions at each site introduce phase errors that cause signal loss for integrations longer than the coherence time of the atmosphere, which typically ranges from 1 s to about 20 s, depending on the weather (Doeleman et al. 2001, 2008). HOPS tasks are designed to deal with data that are segmented on these short timescales, increasing the signal-to-noise ratio (S/N) of detection relative to coherently-integrated data and accounting for amplitude losses due to atmospheric decoherence (Rogers et al. 1995).

Initial baseline fringe fitting was done without segmentation using the HOPS task `fourfit`. Detections with high S/N were used to determine several important quantities for further processing. First, the phase offsets between the 32-MHz channels within each band were determined. Second, approximate atmospheric coherence times maximizing the S/N of detection were calculated to guide further incoherent fringe searching. Third, the residual singleband delay, multiband delay, and delay rate were used to set up narrow search windows for each source to assist in fringe finding.

Scans that produced weak detections or no detection at all were reanalyzed with `fourfit`. Data were then segmented at 4–6 s at a grid of values of multiband delay and delay rate, and the amplitudes were time-averaged at all grid cells. This technique, known as incoherent averaging, allows weaker fringes to be detected in the presence of rapidly variable tropospheric delays. Fi-

nally, detected fringes were segmented at a cadence of 1 s and averaged to produce noise-debiased estimates of the correlation coefficients. Segmented bispectra were also formed and then averaged to construct the closure phase.

The integration time of the incoherent averaging in the final analysis is about 4 minutes per scan for days 88 and 90, 5 minutes for days 91 and 92, and 3 minutes for day 94. All baselines yielded detections on 3C 279 with typical S/Ns of up to 300–400 on the intra-site baselines and 4–6 on the longest baselines (between Arizona and Hawaii). Variations in S/N are mainly due to source structure. However, partially due to known poor atmospheric conditions at some sites, there were some non-detections.

3.1. Issues Relating to the Mixed Hydrogen Maser/Rubidium Setup

The use of the rubidium standard to drive the sampler clocks at CARMA on days 88–92 introduced small delay and frequency drifts into the data. A detailed investigation of affected scans showed that these could be compensated for by introducing an additional multiband delay drift term along with a proportional local oscillator frequency offset. The value of this delay drift was different from scan to scan and ranged in magnitude up to about 32 ps s^{-1} . An analysis of high S/N scans indicated that the delay drift could be characterized as being approximately linear with time over the course of a scan lasting several minutes. A modified version of `fourfit` was produced to allow a user-specified delay drift to be removed before fringe fitting.

Since the same timing references were used at all CARMA telescopes, data on CARMA-CARMA baselines (CD and FD) were unaffected. Additionally, a single delay drift value per scan is sufficient to characterize the effects of this setup for both bands and all baselines including exactly one CARMA station. Determination of delay drift values was done on a scan-by-scan basis by maximizing the S/N of the SMT-CARMA baselines (SD and either SC or SF), which are generally the highest S/N baselines to CARMA due to the fact that the relatively short baseline length does not resolve out as much source emission as the Hawaii-CARMA baselines do.

To the extent that the delay drifts were not linear over the course of a scan, it is possible that the calibrated VLBI amplitudes on the CARMA baselines slightly underestimate the true values. An analysis of the variation of sub-scan delay solutions showed a typical rms scatter of about 0.2 ns during a 4 min scan. The scatter of the delay corresponds to a de-correlation of $\sim 2\%$, caused by a phase change of about 35° across the 480 Hz band, which is less than the uncertainties imposed by calibration.

We verified that closure phases on triangles including a CARMA station are unaffected, since station-based clock errors do not typically introduce non-closing phase errors. The corrections

applied in the modified version of `fourfit` are likewise station-based, so phase rotations applied on one baseline including a CARMA station are exactly compensated by a negative rotation on the other baseline involving CARMA in a triangle. Change of the delay drift around the best-fit values does not introduce significant changes in closure phase. Analysis of sub-scans at shorter intervals with equal duration also show consistency of closure phases with scan-averaged values, indicating that a single delay drift per scan is sufficient. As an example, Figure 1 compares the closure phase of NRAO 530 on days 88-92 with that on day 94 on the SMT-CARMA-Hawaii triangle; Consistent closure phases were measured on the five days of the observation.

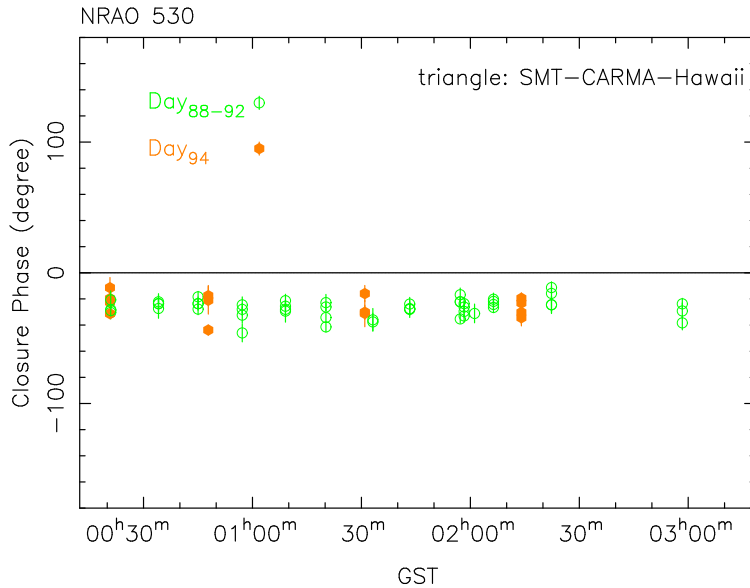


Fig. 1.— Closure phases of NRAO 530 on the SMT-CARMA-Hawaii triangle.

3.2. A Priori Calibration

VLBI correlation coefficients are converted to flux densities by multiplication by the geometric mean of the opacity-corrected system equivalent flux density (SEFD) of the two telescopes on a baseline. The SEFD in turn depends on both the system temperature (T_{sys}) of each scan and the gain of the telescope (or, equivalently, the geometric area and the aperture efficiency).

The aperture efficiencies of the JCMT and the SMT were computed from planet observations in 2009 using a setup identical to the one used for 2011 (Fish et al. 2011). Planet observations were also used to determine the CSO aperture efficiency. System temperatures were obtained using a vane calibration technique. System temperature measurements were taken before each VLBI scan at all sites except at the CSO, where fewer measurements were taken. Comparison of

the measured T_{sys} values at the CSO with those of the nearby JCMT showed a strong correlation, and an empirical fit was used to estimate the system temperature of the CSO when values were missing. System temperatures at CARMA were measured using a chopper wheel before each VLBI scan, then updated continuously during the scan under the assumption that the receiver gain is constant.

Phase switching and lobe rotation were disabled for the single CARMA antennas, preventing simultaneous interferometric and VLBI observations, so SEFDs for stations C and D were determined from CARMA correlator data obtained immediately before each VLBI scan. Self-calibration was used to determine gain corrections for each scan, which were then used to produce an opacity-corrected SEFD. For station F, complex voltage correction factors were calculated from self-calibration every 10 s and used in constructing the phased sum. As a result, the SEFDs for station F implicitly take into account losses due to imperfect phasing. The median phasing efficiency exceeded 70% on days 91 and 94 but was only 50% on day 92 due to increased atmospheric turbulence.

On Mauna Kea the phased array system installed at the SMA aggregated the collecting area of seven SMA antennas with the CSO as the eighth antenna on day 88 and the JCMT as the eighth on the last four days of the observation. The phased array system estimates correcting phases on a scan by scan basis using a seven baseline “calibration correlator”. The phasing efficiency for each calibration correlator frequency is estimated as the absolute value of the vector sum divided by the scalar sum of the calibration correlator visibilities. The sums are taken over the calibration correlator baselines to the reference antenna. These estimated phasing efficiencies for each frequency bin are then averaged over frequency to produce a single phasing efficiency estimate for each calibration correlator scan. An SEFD for the corresponding phased sum ($SEFD_{\text{phased}}$) is computed, by first computing the SEFD for each dish ($SEFD_i$) in the phased array as $SEFD_i = 2 \times T_{\text{sys}_i} \times G_{D_i}$, where T_{sys_i} is the measured DSB system temperature and G_{D_i} is the dish gain (in Janskys per Kelvin) for antenna i . We use measured gain values of 130 Jy/K for each SMA dish, 29.5 Jy/K for the JCMT, and 62.2 Jy/K for the CSO. The SEFD for the phased sum is then computed as $SEFD_{\text{phased}} = (\eta \sum_i \frac{1}{SEFD_i})^{-1}$, where η is the estimated phasing efficiency.

3.3. Flux Density Measurements

In the gaps between VLBI scans, the SMA and CARMA also obtained flux density measurements of target sources. SMA flux densities are available for a subset of sources on days 88, 91, and 92. Titan and MWC 349a were the primary calibrators on days 88 and 92, and constant flux density was assumed for 3C 273 and 3C 274 for primary flux density calibration on day 91 (see [Gurwell et al. 2007](#), for more details). CARMA flux densities are available for most sources on

days 90 and 91¹. Uranus was the primary flux calibrator at CARMA. In Mar/Apr 2011 Uranus was a 3.34×3.27 arcsecond disk, assumed to have a uniform brightness temperature of 102 K. Antenna amplitude gains derived from a self-calibration solution to the Uranus source model were applied to other sources in order to estimate their fluxes. Uranus is much smaller than the primary beamwidths of the CARMA antennas at 229 GHz, which are 30'' and 50'' for the 10-m and 6-m telescopes, respectively. The flux densities derived at CARMA were somewhat higher than those derived at the SMA, by a median value of 8%. This may be because Uranus was observed at the end of the VLBI schedule, after sunrise, when the antenna focus and pointing degrade slightly, or may be due to the uncertainties in the absolute flux scales.

Most of the EHT target sources are pointlike when observed at the resolution of the SMA or CARMA. Each scan with the EHT array includes two high S/N intra-site baselines (JP or OP at Mauna Kea and CD or FD at CARMA). Correlation coefficients measured on the CARMA-CARMA VLBI baseline appear to be a few percent higher than the corresponding correlation coefficient obtained by the CARMA correlator, possibly indicating that the VLBI processing, done with an accumulation period of 1 s, is somewhat more immune to atmospheric coherence losses than the CARMA correlation, which uses an averaging time of 10 s. This is especially true on day 92, when the unstable atmosphere caused the CARMA correlation amplitudes to have a large scatter relative to the VLBI-derived quantities and the CARMA phased array to have correlation coefficients that are biased very low with respect to the VLBI processing.

We have assumed the “zero-spacing” flux densities measured on the intra-site baselines equal to the average of the CARMA interferometer measurements on days 90 and 91.

3.4. Other Known Issues

Two additional instrumental effects are noted with the phased array at the SMA. The a priori amplitudes are corrected for these effects before further processing.

The high-band amplitudes measured on baselines including station P are systemically lower than the low-band amplitudes. The magnitude of this effect is comparable on all baselines to station P, and it is not seen on any other baseline. The source of the high-band loss has not been identified, but could be caused by a gain slope across the band. We have corrected empirically for the loss by multiplying the a priori high-band amplitudes on baselines including station P by the ratio of the low-band and high-band flux densities on the JP baseline (day 88) or OP baseline (days 90–94). Detections on these intra-site baselines have very high S/N, and therefore we do not expect this

¹http://mmarray.org/memos/carma_memo61.pdf

correction to introduce additional errors into the the high-band amplitudes. In the rare instance that neither the JP nor OP baseline is available (for instance, if the other antenna on Mauna Kea missed a scan), the SP baseline is used instead. The average amount of this correction is about 34 %.

Even after correcting the high-band amplitudes, the amplitudes on the XP baseline in both bands are lower than on the XJ or XO baseline, where X represents any other station. The a priori amplitudes on the XP and XJ/XO baselines are tightly correlated, but the XP amplitudes must be increased by an average of 23% for the amplitudes to match. This effect appears to be related to station P rather than either station J or O, as the amplitudes obtained on baselines to station P are lower than the corresponding amplitudes to both station J (on day 88) and station O (on days 90–94). The source of this loss factor is not well understood, but possible reasons may include inaccuracies in calculating the antenna gains and phasing efficiency. We have removed its effect by multiplying all XP amplitudes by 1.23.

3.5. Gain Correction

Calibration is completed by using amplitude self-calibration. For each scan and band, gains are calculated for each station to produce maximal consistency of the data with each other and with the “zero-spacing” flux densities measured with the SMA and CARMA. The method is similar to that described in [Fish et al. \(2011\)](#), except that all baselines are used and weighted by the data S/N in computing the gain correction coefficients. After gain correction, the calibrated intra-site VLBI amplitudes (e.g., CD) are equal to the flux density measured by CARMA, and amplitudes of substantively identical VLBI quantities (e.g., SC and SD, low and high bands) are made as equal as possible.

4. Results

4.1. Source Structure Modeling at 1.3 mm

The calibrated amplitudes and closure phases (Tables 2 and 3) are shown in Figures 2 and 3, respectively. Trivial triangles, which involve an intra-site baseline (JP or OP at Mauna Kea and CD or FD at CARMA), have essentially zero closure phase, indicating a point-like structure at the resolution provided by the intra-site baselines (a few arc seconds).

The source structure at 1.3 mm was quantitatively parameterized by considering a class of simple circular Gaussian models that fit the calibrated amplitudes and closure phase jointly following [Lu et al. \(2012\)](#). Uncertainties are reported based on the size of the region around the

Table 2: Gain-corrected Visibility Amplitudes of 3C 279

Day	hh	mm	Baseline	u (M λ)	v (M λ)	Flux Density (Jy)	σ (Jy)	Band
88	07	26	CD	-0.006	-0.073	13.83	0.18	high
	07	26	SC	-526.942	283.963	6.14	0.12	high
	07	26	SD	-526.948	283.889	6.14	0.11	high
	08	34	CD	0.011	-0.074	13.83	0.20	high
	08	34	CJ	-2794.721	-1298.854	1.17	0.15	high
	08	34	CP	-2794.731	-1298.751	1.12	0.14	high
	08	34	DJ	-2794.732	-1298.780	1.01	0.14	high
	08	34	DP	-2794.742	-1298.678	1.06	0.12	high
	08	34	JP	-0.010	0.103	13.83	0.06	high
	08	34	SC	-598.012	300.969	5.20	0.14	high

A portion of this table is shown here to demonstrate its form and content. An online machine-readable version of the full table is available.

Table 3: Closure phases of 3C 279

Day	hh	mm	Triangle	Closure Phase (Degree)	σ (Degree)	Band
88	08	34	CDP	-11.9	5.8	high
	09	32	CDP	-1.8	4.1	high
	08	34	CDJ	-0.3	5.6	high
	09	32	CDJ	-2.5	6.0	high
	10	01	CDJ	1.2	4.0	high
	08	34	CJP	-3.2	7.2	high
	09	32	CJP	2.7	4.7	high
	08	34	DJP	3.7	4.5	high
	09	32	DJP	1.1	4.1	high
	10	01	DJP	4.9	3.5	high

A portion of this table is shown here to demonstrate its form and content. An online machine-readable version of the full table is available.

best-fit point in parameter space corresponding to 68.3 % probability and the true uncertainties may be somewhat larger. Model fitting was performed for the data on days 88–92 and day 94 separately, because the closure phase on the non-trivial triangles (SMT-CARMA-Hawaii) on day 94 is significantly different than on the other four days (Figures 2 and 3, lower right). Closure phases on other triangles (e.g., CARMA-Hawaii-Hawaii), and for all the other sources on all triangles do not show any sign of change in a similar manner and we do not believe that this change is due to calibration uncertainties (§ 3.1).

We started the model fitting with a two-component model since a single-component model is completely ruled out by the measured nonzero closure phase on the non-trivial triangles. A two-component model (model Ma) yielded a good fit to the amplitudes and nonzero closure phases, representing the most basic structure of the emission. The structure is characterized by a compact, but relatively weak component (A0), and a stronger component (A1) $\sim 130\text{--}140 \mu\text{as}$ away at a PA of about -50° (Table 4). The measured closure phases remove the 180° of degeneracy in the jet position angle. The two models of $\text{Ma}_{88\text{--}92}$ and Ma_{94} are very similar to each other, and both indicate a jet direction (regardless of core identification) very different from the typical centimeter jet orientation (i.e., extending to the southwest).

Although the two-component models adequately fit the data, it is interesting to know to what extent a slightly more complicated, three-component model can be constrained. This is encouraged by a few indications that the source structure may be more complicated than assumed, for instance, the two-component model seems to slightly over-predict the flux density on SMT-Hawaii baselines around $23^{\text{h}}00$ (Figure 2, upper right panel) and underestimates the non-trivial closure phase at the end of observations on day 94 (Figure 3, lower right). For the three-component model (Table 4), a few parameters are not well constrained, e.g., the position of the component Mb(2), for both data sets. We therefore introduced an a priori constraint for the position angle of this component (-120° , relative to Mb(0)) according to models of the 7 mm VLBI images (Section 4.2). We also noticed that there are regions in the parameter space that provide alternative three-component models. These three-component models, however, are indistinguishable from the pure perspective of χ^2 , indicating that they are only at a marginal level of detail that the current data can support.

4.2. Source Structure at 7 mm

At 7 mm, the Boston University group monitored 3C 279 with the VLBA roughly monthly. These data have been reduced in the same manner as described in Jorstad et al. (2005) and will be presented in Jorstad et al. (in prep). We turned to these data to check the consistency of the modeled structure at 1.3 mm after initial model fitting. The images at epochs that bracket the EHT observations begin to show some asymmetry in the core region, evident by the small, but nonzero

Table 4: Model-fit parameters for 1.3 mm VLBI observations of 3C 279.

Model	χ^2_ν	ID	Flux Density (Jy)	Radius (μas)	PA (degree)	Size (FWHM) μas	T_b (K)
two-component model (model A)							
Ma _{88–92}	2.0	0	3.8 ± 0.3	0	0	42 ± 3	7.7×10^{10}
		1	10.0 ± 0.4	133 ± 6	-54 ± 5	73 ± 3	6.7×10^{10}
Ma ₉₄	1.8	0	4.0 ± 0.4	0	0	42 ± 2	8.1×10^{10}
		1	9.8 ± 0.3	145 ± 7	-52 ± 4	64 ± 3	8.5×10^{10}
three-component model (model B)							
Mb _{88–92}	1.4	0	1.2 ± 0.5	0	0	13 ± 9	2.5×10^{11}
		1	1.0 ± 0.4	110 ± 20	-35 ± 3	17 ± 11	1.2×10^{11}
		2	11.6 ± 1.0	79 ± 29	-120^a	168 ± 5	1.5×10^{10}
Mb ₉₄	1.0	0	1.4 ± 0.4	0	0	11 ± 11	4.1×10^{11}
		1	1.2 ± 0.4	91 ± 24	-37 ± 6	13 ± 11	2.6×10^{11}
		2	11.2 ± 0.7	94 ± 34	-120^a	184 ± 9	1.2×10^{10}

^a fixed during model fitting

closure phases on the triangles involving the longest VLBA baselines (~ 0.1 mas resolution). The 2011 April 22 observations at 7 mm are at the epoch closest to the 1.3 mm observations (separated by 22 days). Figure 4 (left) shows the 7 mm VLBA image at this epoch, which reveals a triple structure at the central region. The properties of the two compact components (relative position and sizes) at 7 mm in the central region show remarkable similarity to those of component A0 and A1 (Figure 4, right) with flux densities of 8.8 and 6.1 Jy. For a three-component model at 1.3 mm, it is reasonable to assume that B2 corresponds to the extended component at 7 mm and have similar position given their similar size. Once the a priori PA constraint (similar PA as at 7 mm) is introduced for component B2, the separation between B2 and B0 shows good consistency with the 7 mm results.

5. Discussion

The present 1.3 mm VLBI observations reveal a jet structure of 3C 279 (Figure 5) very different from the typical jet direction (i.e., towards south-west) at centimeter wavelengths (e.g., Jorstad et al. 2005). The component A1 is likely to be the core, a compact feature located at the upstream end of jets as seen in VLBI images. The nonsimultaneous two-frequency spectral indices α ($S \propto \nu^\alpha$) between 43 and 230 GHz are 0.3 and -0.5 for A1 and A0, suggesting A1 is the core

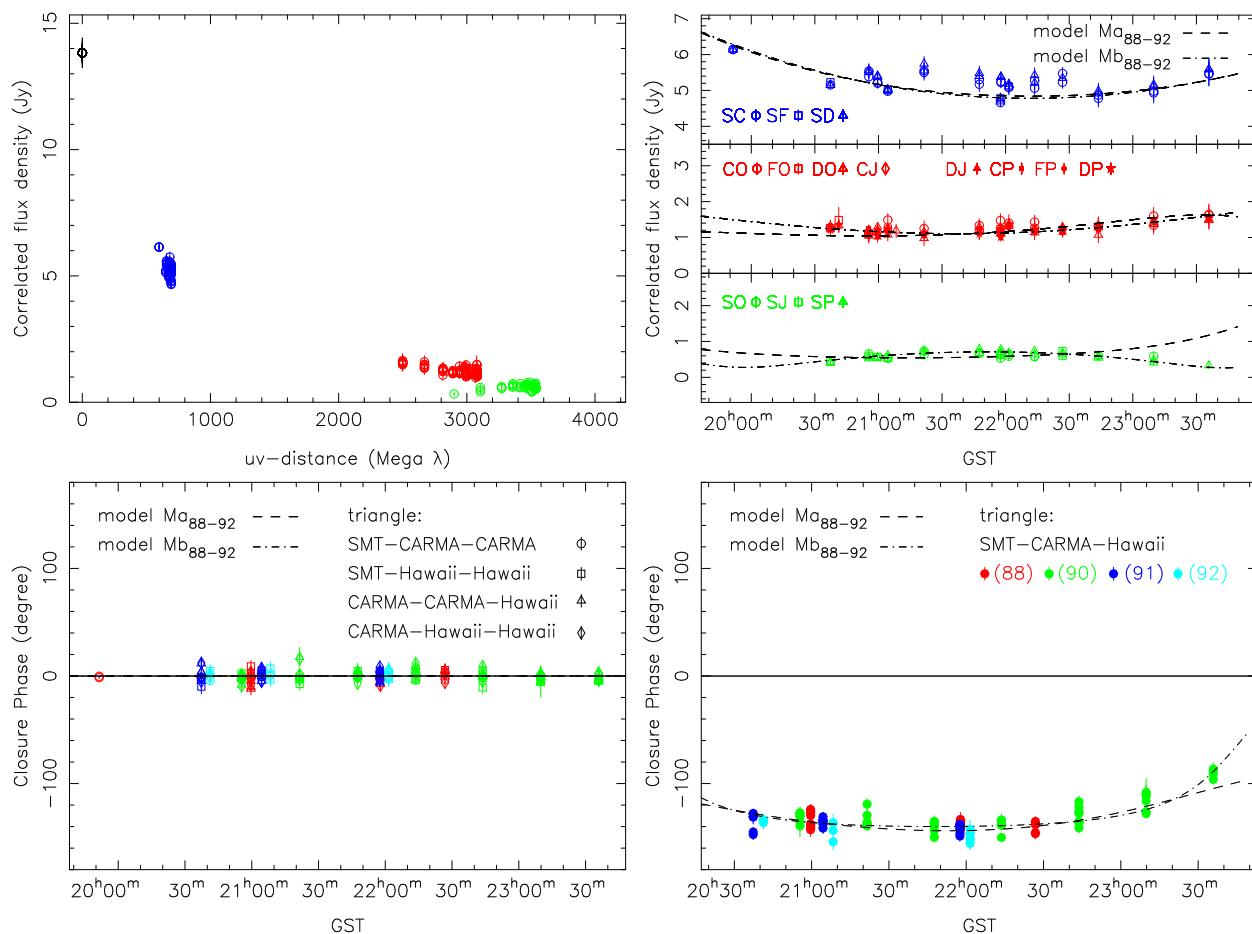


Fig. 2.— Measured correlated flux density and closure phase for days 88–92. Upper panel (left): correlated flux density as a function of uv distance. Since the source structure is not circularly symmetric, the correlated flux density will change for a given uv distance as the Earth rotates. Upper panel (right): correlated flux density as a function of time with comparison of the two models shown in Table 4. The correlated flux densities are color-coded by baseline. Lower panels: closure phase as function of time for the trivial triangles (left), which include an intra-site baseline, and non-trivial triangles (right). Detections are color-coded by observing epoch, as indicated in the legend in the lower right panel. The predicted closure phases of the two models (Table 4) are also shown.

with a flat spectrum, while A0 is optically thin. Determination of the spectral index using data at two frequencies is not a robust estimate hence future high resolution multi-frequency observations are needed to measure the spectral properties and further confirm this scenario. This identification gives an inner jet PA (i.e., the PA of A0 with respect to the core A1) of $\simeq 127^\circ \pm 3^\circ$.

The repeat of observations on successive days in the same GST range permits us to investi-

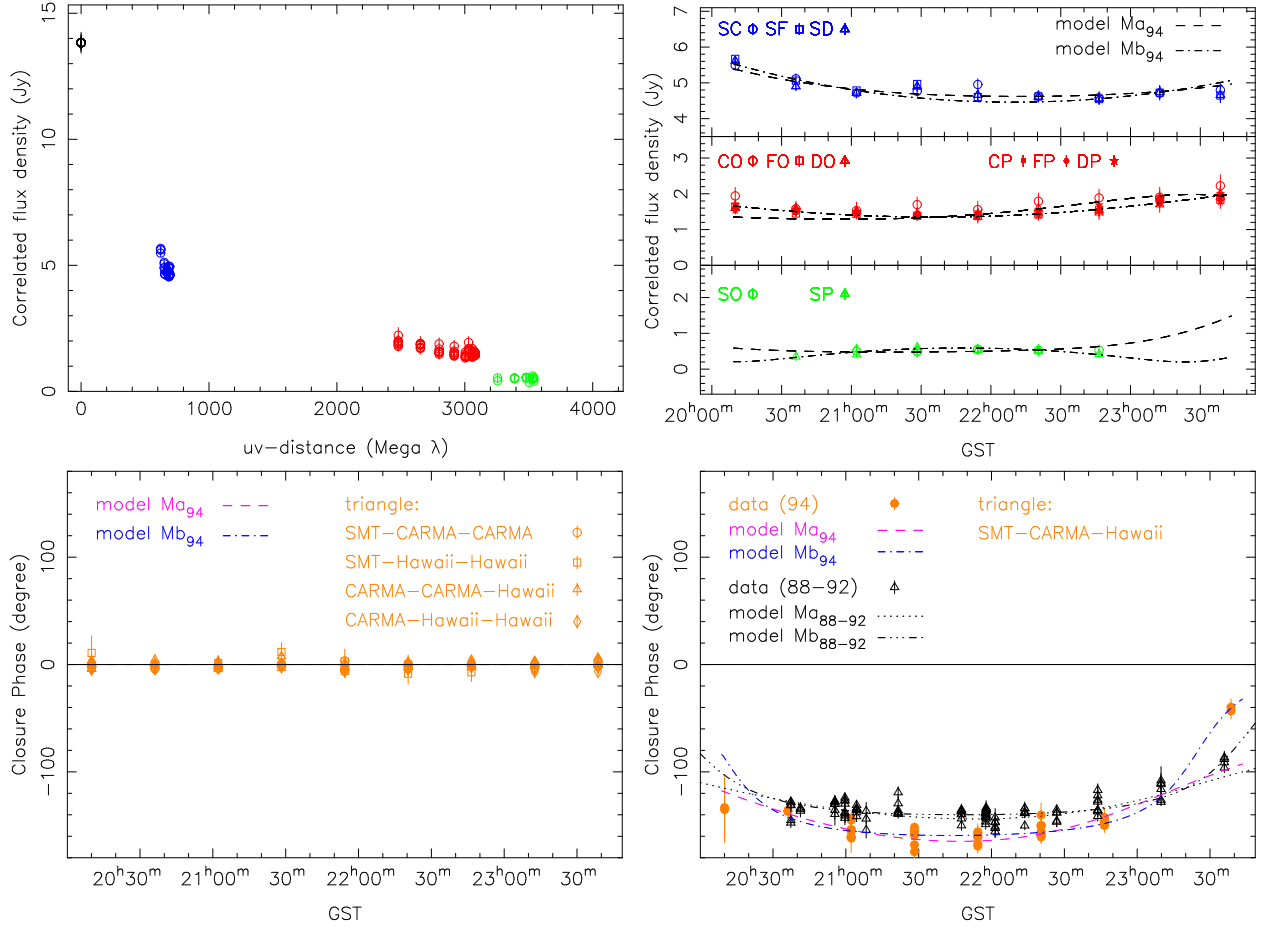


Fig. 3.— Same as Figure 2, but for day 94. Note that the closure phase data and models for the SMT-CARMA-Hawaii triangle on days 88–92 are overplotted for comparison (lower right, open symbols).

gate the possible daily variations of flux density and structure of 3C 279. For other blazars, like NRAO 530, the inner jet components were found to be more variable than those further out on daily timescales (Lu et al. 2011). The change of closure phases on day 94 provides an opportunity to study the interday variability of 3C 279 on sub-pc scales, which can be caused, e.g., by a component brightening. From Table 4, it seems that the closure phase change can be explained via a small change of source structure and variations in how the total flux is divided up, but it cannot be unambiguously attributed to a single model parameter. Observations at 7 mm clearly show that A0 is swinging in position angle and moving southwest relative to A1 (Jorstad et al. in prep). In view of these fast changes, more frequent monitoring is needed in the future to follow up these variations.

Jet components in 3C 279 were known to have notably different speeds and position an-

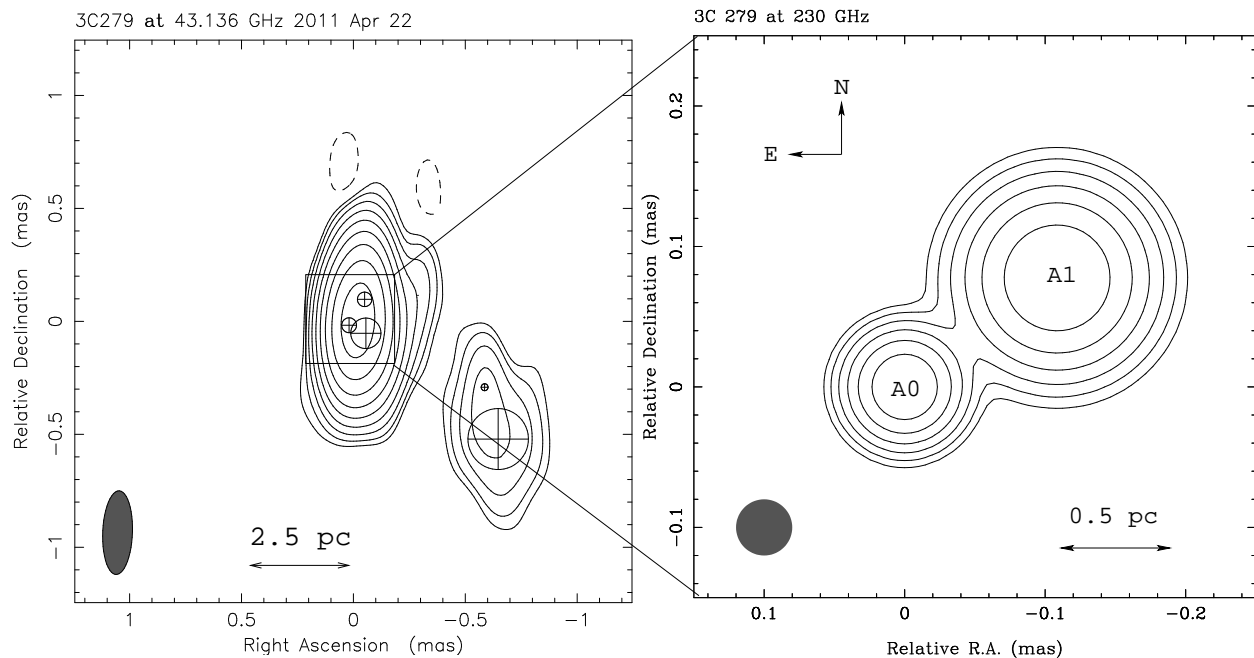


Fig. 4.— Left: Total intensity image of 3C 279 at 7 mm obtained on 2011 April 22 with model-fit components superimposed (Jorstad et al. in prep). The peak flux density is $15.6 \text{ Jy beam}^{-1}$ and contours are drawn at -0.25% , 0.25% , 0.5% , 1% , 2% , 4% , 8% , 26% , 32% , and 64% of the peak. The beam size is approximately $0.37 \times 0.13 \text{ mas}$ at a position angle of -2° . Right: model image of 3C 279 at 1.3 mm based on data from days 88-92 (model Ma_{88-92}). The image is convolved with a circular beam with an FWHM of $20 \mu\text{as}$. Contours are drawn beginning at 1.6% of the peak brightness of 0.7 Jy/beam and increase by a factor of 2.

gles (e.g., Wehrle et al. 2001; Jorstad et al. 2004; Chatterjee et al. 2008). This has been interpreted as a consequence of a precessing jet by Abraham & Carrara (1998). Recently, Qian (2011, 2012) proposed a jet-nozzle precession model for 3C 279, in which the jet components move along a common (collimated) curved trajectory precessing with a period of ~ 25 yrs. They predicted the jet ejection angle approaching $\sim -90^\circ \pm 10^\circ$ in 2010-2012. The inner jet position angle seen with 1.3 mm VLBI is beyond the range of the PA that these models predict (between $\sim -155^\circ$ and $\sim -80^\circ$). It should be pointed out that estimating the ejection position angle and time of component B0 is not a straightforward task due to its swing. More erratic changes in apparent speed and direction may naturally result from a small change in the viewing angle (Homan et al. 2003; Jorstad et al. 2004). The new inner jet direction seen with 1.3 mm VLBI is probably a similar event, suggesting that the jet points very close to our line of sight. However, the origin of these changes of the jet is still an open question.

Past centimeter VLBI observations have shown that the core of 3C 279 has brightness temper-

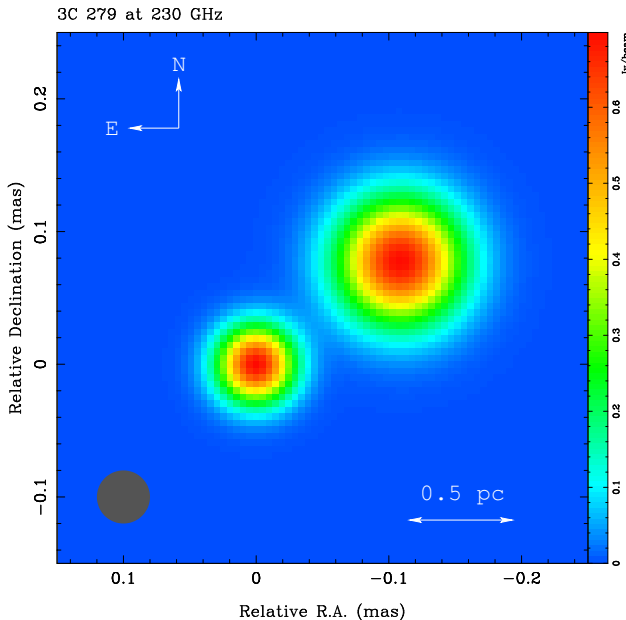


Fig. 5.— The inner jet structure of 3C 279 at 1.3 mm based on data from days 88-92 (model Ma_{88-92}). The image is convolved with a circular beam with an FWHM of $20\mu\text{as}$ and the vertical color bar on the right has units Jy/beam.

ature $> 10^{12}$ K (e.g., Piner et al. 2000; Wehrle et al. 2001, and references therein). Recently, Lee et al. (2008) suggested a systematic decrease of jet brightness temperature in compact radio sources towards the mm-VLBI core at 3.5 mm. In the quasar 1921-293, the low brightness temperature of the 1.3 mm core is consistent with this trend (Lu et al. 2012). For 3C 279, the measured brightness temperature towards the VLBI core at 1.3 mm is consistent with a lower value of $\sim 8 \times 10^{10}$ K.

We expect future observations with improved uv coverage and sensitivity to provide stricter constraints on the model. Introducing a priori knowledge is able to help models converge, but solutions are non-unique. Moreover, it is not straightforward to do so for current observations due to the fast structure change on the probed spatial scales (sub-parsec for 3C 279) and the lack of observations that are close in time and with matched angular resolution. This situation, however, is expected to change soon.

With the planned improvement of millimeter VLBI capability over the next few years, the EHT will allow direct imaging of these inner regions close to the jet origin and will be able to discriminate between these models. Here we consider two synthetic data sets using models Ma_{88-92} and Mb_{88-92} as input for future observations of 3C 279 with seven potential stations (Doeleman et al. 2009; Fish et al. 2009): Hawaii, consisting of one or more of the JCMT and SMA phased

together into a single aperture; the SMT; CARMA; the Large Millimeter Telescope (LMT) on Sierra Negra, Mexico; the phased Atacama Large Millimeter/submillimeter Array (ALMA); the Institut de Radioastronomie Millimétrique (IRAM) 30 m telescope on Pico Veleta (PV), Spain; and the IRAM Plateau de Bure (PdB) Interferometer, phased together as a single aperture. Assumed telescope sensitivities are updated from [Doeleman et al. \(2009\)](#). For our simulations, we took phased ALMA as the site in Chile. We note that early imaging studies at 1.3 mm will likely involve the APEX 12 m dish, which would sample similar spatial frequencies to the phased ALMA.

The array used in this simulation provides very good uv coverage on 3C 279 (Figure 6), indicating sufficient imaging capabilities in the near future. We show in Figure 7 (left) the predicted visibility amplitudes and the expected closure phases on the SMT-CARMA-LMT triangle as an example (Figure 7, right) for the two models. These models predict different behavior for most of the baselines and triangles, and they can be straightforwardly discriminated. Since these models may be approximating a continuous expanding jet, future observation will enable the direct imaging of the jet structure with improved sensitivity and uv coverage in the coming years.

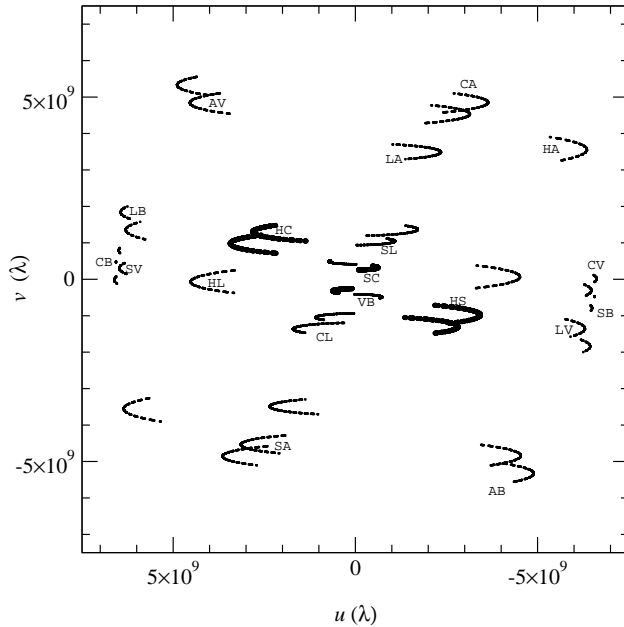


Fig. 6.— uv coverage for the array used for the simulation. Tracks are labeled by baseline (H: Hawaii; S: SMT; C: CARMA; L: LMT; A: ALMA; V: Pico Veleta; B: Plateau de Bure Interferometer). The visibility at $(-u, -v)$ is the complex conjugate of that at (u, v) . uv tracks for the baselines in the 2011 observations are highlighted.

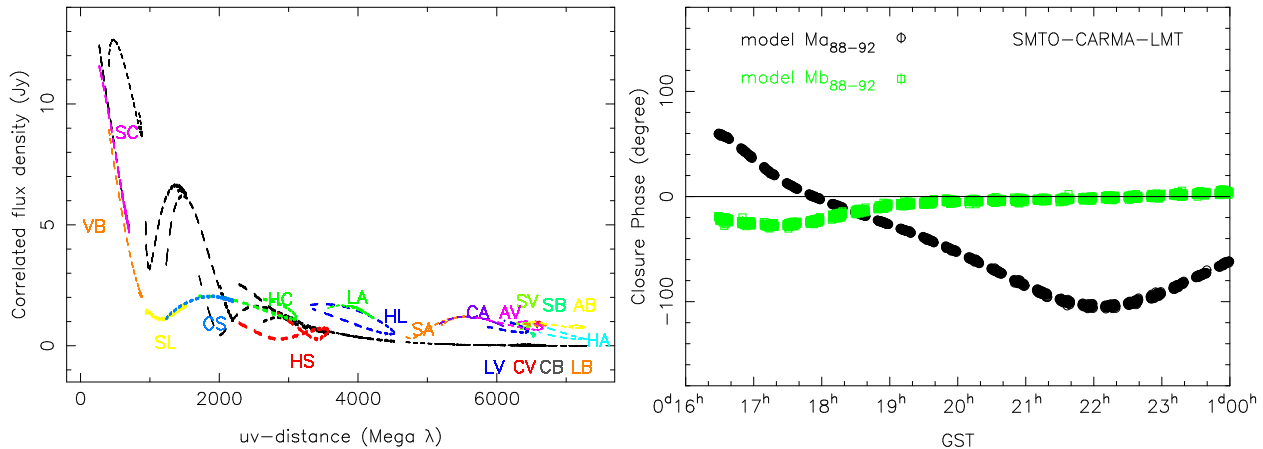


Fig. 7.— Left: correlated flux density as a function of uv distance for the two models of days 88-92 (Ma_{88-92} and Mb_{88-92} , Table 4). Points for the model Mb_{88-92} are color-coded and labeled by baseline (same as in Figure 6). Right: plot of the predicted closure phase for the shown time range on the SMT-CARMA-LMT triangle. Simulated data were coherently averaged into 10-s bins.

6. Conclusions

We have presented the first high-resolution VLBI observations of 3C 279 at 230 GHz. The sub-parsec-scale emission is dominated by a compact double structure along the northwest-southeast direction. We find radio structures at 1.3 mm similar to those that were seen in the central core regions of 7 mm super-resolution images. The change of closure phases on the last day during our observations provides opportunities to study sub-parsec-scale jet structure change on daily timescales. If further confirmed by future investigations, it can help us locate and understand the physical process behind these rapid variations.

During our observations, 3C 279 showed an unusual inner jet direction, inconsistent with the prediction of jet precession models by Qian (2011, 2012). The new jet direction, along with the swing (i.e., motion of component A0 along a non-radial trajectory) of the inner jet seen with 43 GHz data (Jorstad et al. in prep), reflects the non-ballistic nature of the jet and raise the possibility that this phenomenon is associated with a process erratic in nature, similar to the jet of OJ 287 (Agudo et al. 2012). Our results indicate that the core brightness temperature at λ 1.3 mm is significantly lower than at longer wavelengths (e.g., Piner et al. 2000). With better uv coverage and sensitivity in the very near future, it is obvious that VLBI at 1.3 mm will be able to directly image the sub-parsec scale emission.

High-frequency VLBI work at MIT Haystack Observatory is supported by grants from the National Science Foundation (NSF). The Submillimeter Array is a joint project between the Smithso-

nian Astrophysical Observatory and the Academia Sinica Institute of Astronomy and Astrophysics and is funded by the Smithsonian Institution and the Academia Sinica. High-frequency VLBI work at the Arizona Radio Observatory is partially supported through the NSF ATI (AST-0905844) and URO (AST-1140030) programs. This study makes use of 43 GHz VLBA data from the Boston University gamma-ray blazar monitoring program (<http://www.bu.edu/blazars/VLBAproject.html>), funded by NASA through the Fermi Guest Investigator Program. The National Radio Astronomy Observatory is a facility of the National Science Foundation operated under cooperative agreement by Associated Universities, Inc. L.L. acknowledges the financial support of CONACyT, Mexico (project 104497) DGAPA, UNAM (project IN118110) and the John Simon Guggenheim Memorial Foundation (Fellowship 2010-2011)

Facilities: ARO SMT, CARMA, CSO, JCMT, SMA, VLBA

REFERENCES

- Abraham, Z., & Carrara, E. A. 1998, *ApJ*, 496, 172
- Agudo, I., Marscher, A. P., Jorstad, S. G., et al. 2012, *ApJ*, 747, 63
- Attridge, J. M. 2001, *ApJ*, 553, L31
- Bloom, S. D., Fromm, C. M., & Ros, E. 2013, *AJ*, 145, 12
- Chatterjee, R., Jorstad, S. G., Marscher, A. P., et al. 2008, *ApJ*, 689, 79
- Cheung, C. C. 2002, *ApJ*, 581, L15
- Cohen, M. H., Cannon, W., Purcell, G. H., et al. 1971, *ApJ*, 170, 207
- Collmar, W., Böttcher, M., Krichbaum, T. P., et al. 2010, *A&A*, 522, A66
- Cotton, W. D., Counselman, C. C., III, Geller, R. B., et al. 1979, *ApJ*, 229, L115
- de Pater, I., & Perley, R. A. 1983, *ApJ*, 273, 64
- Doeleman, S. S., Fish, V. L., Broderick, A. E., Loeb, A., & Rogers, A. E. E. 2009, *ApJ*, 695, 59
- Doeleman, S. S., Fish, V. L., Schenck, D. E., et al. 2012, *Science*, 338, 355
- Doeleman, S. S., Shen, Z.-Q., Rogers, A. E. E., et al. 2001, *AJ*, 121, 2610
- Doeleman, S. S., Weintroub, J., Rogers, A. E. E., et al. 2008, *Nature*, 455, 78

- Fish, V. L., Broderick, A. E., Doeleman, S. S., & Loeb, A. 2009, *ApJ*, 692, L14
- Fish, V. L., Doeleman, S. S., Beaudoin, C., et al. 2011, *ApJ*, 727, L36
- Greve, A., Könönen, P., Graham, D. A., et al. 2002, *A&A*, 390, L19
- Gurwell, M. A., Peck, A. B., Hostler, S. R., Darrah, M. R., & Katz, C. A. 2007, *From Z-Machines to ALMA: (Sub)Millimeter Spectroscopy of Galaxies*, 375, 234
- Hayashida, M., Madejski, G. M., Nalewajko, K., et al. 2012, *ApJ*, 754, 114
- Homan, D. C., Lister, M. L., Kellermann, K. I., et al. 2003, *ApJ*, 589, L9
- Homan, D. C., Lister, M. L., Aller, H. D., Aller, M. F., & Wardle, J. F. C. 2009, *ApJ*, 696, 328
- Jorstad, S. G., Marscher, A. P., Mattox, J. R., et al. 2001, *ApJS*, 134, 181
- Jorstad, S. G., Marscher, A. P., Lister, M. L., et al. 2004, *AJ*, 127, 3115
- Jorstad, S. G., Marscher, A. P., Lister, M. L., et al. 2005, *AJ*, 130, 1418
- Jorstad, S. G., et al., 2013, in prep.
- Krichbaum, T. P., Graham, D. A., Greve, A., et al. 1997, *A&A*, 323, L17
- Larionov, V. M., Jorstad, S. G., Marscher, A. P., et al. 2008, *A&A*, 492, 389
- Lee, S.-S., Lobanov, A. P., Krichbaum, T. P., et al. 2008, *AJ*, 136, 159
- Leppänen, K. J., Zensus, J. A., & Diamond, P. J. 1995, *AJ*, 110, 2479
- Lu, R.-S., Krichbaum, T. P., & Zensus, J. A. 2011, *MNRAS*, 418, 2260
- Lu, R.-S., Fish, V. L., Weintroub, J., et al. 2012, *ApJ*, 757, L14
- Marziani, P., Sulentic, J. W., Dultzin-Hacyan, D., Calvani, M., & Moles, M. 1996, *ApJS*, 104, 37
- Pauliny-Toth, I. I. K., Preuss, E., Witzel, A., et al. 1981, *AJ*, 86, 371
- Pearson, T. J. 1995, in *ASP Conf. Ser. 82, Very Long Baseline Interferometry and the VLBA*, ed., J. A. Zensus, P. J. Diamond, & P. J. Napier (San Francisco, CA: ASP), 268
- Piner, B. G., Edwards, P. G., Wehrle, A. E., et al. 2000, *ApJ*, 537, 91
- Piétu, V., di Folco, E., Guilloteau, S., Gueth, F., & Cox, P. 2011, *A&A*, 531, L2
- Qian, S.-J. 2011, *Research in Astronomy and Astrophysics*, 11, 43

- Qian, S.-J. 2012, *Research in Astronomy and Astrophysics*, 12, 46
- Rogers, A. E. E., Doeleman, S. S., & Moran, J. M. 1995, *AJ*, 109, 1391
- Taylor, G. B. 2000, *ApJ*, 533, 95
- Unwin, S. C., Cohen, M. H., Hodges, M. W., Zensus, J. A., & Biretta, J. A. 1989, *ApJ*, 340, 117
- Wardle, J. F. C., Homan, D. C., Ojha, R., & Roberts, D. H. 1998, *Nature*, 395, 457
- Wehrle, A. E., Piner, B. G., Unwin, S. C., et al. 2001, *ApJS*, 133, 297
- Whitney, A. R., Shapiro, I. I., Rogers, A. E. E., et al. 1971, *Science*, 173, 225
- Zavala, R. T., & Taylor, G. B. 2001, *ApJ*, 550, L147

Table 5:: Gain-corrected Visibility Amplitudes of 3C 279

Day	hh	mm	Baseline	u (M λ)	v (M λ)	Flux Density (Jy)	σ (Jy)	Band
88	07	26	CD	-0.006	-0.073	13.83	0.18	high
	07	26	SC	-526.942	283.963	6.14	0.12	high
	07	26	SD	-526.948	283.889	6.14	0.11	high
	08	34	CD	0.011	-0.074	13.83	0.20	high
	08	34	CJ	-2794.721	-1298.854	1.17	0.15	high
	08	34	CP	-2794.731	-1298.751	1.12	0.14	high
	08	34	DJ	-2794.732	-1298.780	1.01	0.14	high
	08	34	DP	-2794.742	-1298.678	1.06	0.12	high
	08	34	JP	-0.010	0.103	13.83	0.06	high
	08	34	SC	-598.012	300.969	5.20	0.14	high
	08	34	SD	-598.000	300.895	5.41	0.13	high
	08	34	SJ	-3392.733	-997.886	0.56	0.10	high
	08	34	SP	-3392.742	-997.783	0.56	0.10	high
	09	32	CD	0.026	-0.074	13.83	0.21	high
	09	32	CJ	-2731.032	-1227.751	1.09	0.15	high
	09	32	CP	-2731.056	-1227.648	1.14	0.12	high
	09	32	DJ	-2731.058	-1227.677	1.13	0.13	high
	09	32	DP	-2731.082	-1227.574	1.01	0.11	high

Table 5 – continued

Day	hh	mm	Baseline	u (M λ)	v (M λ)	Flux Density (Jy)	σ (Jy)	Band
09	32		JP	-0.024	0.103	13.83	0.05	high
09	32		SC	-617.224	316.606	5.25	0.15	high
09	32		SD	-617.199	316.532	5.38	0.14	high
09	32		SJ	-3348.256	-911.145	0.64	0.10	high
09	32		SP	-3348.280	-911.042	0.70	0.08	high
10	01		CD	0.032	-0.074	13.83	0.23	high
10	01		CJ	-2632.888	-1193.380	1.25	0.15	high
10	01		DJ	-2632.921	-1193.306	1.15	0.14	high
10	01		DP	-2632.952	-1193.202	1.21	0.11	high
10	01		JP	-0.031	0.104	13.83	0.05	high
10	01		SC	-611.983	324.482	5.23	0.17	high
10	01		SD	-611.951	324.408	5.34	0.16	high
10	01		SJ	-3244.871	-868.898	0.73	0.10	high
10	01		SP	-3244.902	-868.794	0.69	0.08	high
07	26		CD	-0.006	-0.073	13.83	0.16	low
07	26		SC	-526.942	283.963	6.14	0.12	low
07	26		SD	-526.948	283.889	6.14	0.11	low
08	34		CD	0.011	-0.074	13.83	0.19	low
08	34		CJ	-2794.721	-1298.854	1.25	0.14	low
08	34		CP	-2794.731	-1298.751	1.21	0.10	low
08	34		DJ	-2794.732	-1298.780	1.11	0.14	low
08	34		DP	-2794.742	-1298.678	1.19	0.10	low
08	34		JP	-0.010	0.103	13.83	0.05	low
08	34		SC	-598.012	300.969	5.23	0.13	low
08	34		SD	-598.000	300.895	5.38	0.12	low
08	34		SJ	-3392.733	-997.886	0.57	0.10	low
08	34		SP	-3392.742	-997.783	0.55	0.07	low
09	32		CD	0.026	-0.074	13.83	0.19	low
09	32		CJ	-2731.032	-1227.751	1.17	0.14	low
09	32		CP	-2731.056	-1227.648	1.07	0.10	low
09	32		DJ	-2731.058	-1227.677	1.08	0.12	low
09	32		DP	-2731.082	-1227.574	1.03	0.09	low
09	32		JP	-0.024	0.103	13.83	0.04	low
09	32		SC	-617.224	316.606	5.22	0.15	low
09	32		SD	-617.199	316.532	5.38	0.13	low

Table 5 – continued

Day	hh	mm	Baseline	u (M λ)	v (M λ)	Flux Density (Jy)	σ (Jy)	Band
	09	32	SJ	-3348.256	-911.145	0.65	0.10	low
	09	32	SP	-3348.280	-911.042	0.78	0.06	low
	10	01	CD	0.032	-0.074	13.83	0.22	low
	10	01	CJ	-2632.888	-1193.380	1.21	0.14	low
	10	01	CP	-2632.919	-1193.276	1.13	0.11	low
	10	01	DJ	-2632.921	-1193.306	1.15	0.12	low
	10	01	DP	-2632.952	-1193.202	1.18	0.09	low
	10	01	JP	-0.031	0.104	13.83	0.04	low
	10	01	SC	-611.983	324.482	5.47	0.17	low
	10	01	SJ	-3244.871	-868.898	0.59	0.11	low
	10	01	SP	-3244.902	-868.794	0.64	0.08	low
90	08	22	CD	0.010	-0.074	13.83	0.32	high
	08	22	CO	-2792.305	-1303.980	1.12	0.22	high
	08	22	CP	-2792.411	-1303.851	1.24	0.10	high
	08	22	DO	-2792.316	-1303.906	1.05	0.20	high
	08	22	DP	-2792.421	-1303.777	1.18	0.09	high
	08	22	OP	-0.106	0.129	13.83	0.04	high
	08	22	SC	-595.149	299.879	5.38	0.20	high
	08	22	SD	-595.138	299.806	5.56	0.18	high
	08	22	SO	-3387.454	-1004.100	0.65	0.12	high
	08	22	SP	-3387.560	-1003.971	0.53	0.06	high
	08	48	CD	0.017	-0.074	13.83	0.34	high
	08	48	CO	-2791.661	-1271.908	1.25	0.21	high
	08	48	CP	-2791.781	-1271.778	1.06	0.11	high
	08	48	DO	-2791.677	-1271.835	0.98	0.21	high
	08	48	DP	-2791.797	-1271.705	1.07	0.10	high
	08	48	OP	-0.120	0.130	13.83	0.04	high
	08	48	SC	-609.874	306.800	5.50	0.22	high
	08	48	SD	-609.857	306.727	5.75	0.20	high
	08	48	SO	-3401.534	-965.108	0.63	0.13	high
	08	48	SP	-3401.654	-964.978	0.70	0.06	high
	09	14	CD	0.023	-0.074	13.83	0.36	high
	09	14	CO	-2754.929	-1240.052	1.17	0.23	high
	09	14	CP	-2755.061	-1239.921	1.25	0.10	high
	09	14	DO	-2754.952	-1239.978	1.16	0.22	high

Table 5 – continued

Day	hh	mm	Baseline	u (M λ)	v (M λ)	Flux Density (Jy)	σ (Jy)	Band
09	14		DP	-2755.085	-1239.847	1.10	0.10	high
09	14		OP	-0.133	0.132	13.83	0.04	high
09	14		SC	-616.715	313.845	5.17	0.21	high
09	14		SD	-616.692	313.771	5.48	0.20	high
09	14		SO	-3371.644	-926.207	0.68	0.12	high
09	14		SP	-3371.777	-926.075	0.68	0.05	high
09	40		CD	0.029	-0.074	13.83	0.38	high
09	40		CO	-2682.585	-1208.822	1.26	0.23	high
09	40		CP	-2682.728	-1208.689	1.18	0.13	high
09	40		DO	-2682.614	-1208.748	1.25	0.20	high
09	40		DP	-2682.758	-1208.615	1.23	0.11	high
09	40		OP	-0.144	0.133	13.83	0.04	high
09	40		SC	-615.585	320.923	5.28	0.23	high
09	40		SD	-615.555	320.849	5.21	0.20	high
09	40		SO	-3298.170	-887.899	0.58	0.12	high
09	40		SP	-3298.313	-887.766	0.64	0.07	high
10	10		CD	0.036	-0.075	13.83	0.41	high
10	10		CO	-2556.104	-1174.093	1.32	0.25	high
10	10		CP	-2556.258	-1173.958	1.35	0.15	high
10	10		DO	-2556.140	-1174.018	1.28	0.22	high
10	10		DP	-2556.294	-1173.883	1.25	0.14	high
10	10		OP	-0.154	0.135	13.83	0.05	high
10	10		SC	-604.399	329.011	4.78	0.24	high
10	10		SD	-604.363	328.936	4.99	0.22	high
10	10		SP	-3160.656	-844.947	0.59	0.08	high
10	36		CD	0.041	-0.075	13.83	0.46	high
10	36		CO	-2410.818	-1145.566	1.60	0.24	high
10	36		CP	-2410.978	-1145.429	1.48	0.14	high
10	36		DO	-2410.859	-1145.490	1.37	0.22	high
10	36		DP	-2411.019	-1145.354	1.49	0.12	high
10	36		OP	-0.161	0.137	13.83	0.04	high
10	36		SC	-586.281	335.849	4.93	0.28	high
10	36		SD	-586.240	335.774	5.16	0.25	high
10	36		SP	-2997.260	-809.579	0.41	0.09	high
11	02		CD	0.046	-0.076	13.83	0.59	high

Table 5 – continued

Day	hh	mm	Baseline	u (M λ)	v (M λ)	Flux Density (Jy)	σ (Jy)	Band
11	02		CO	-2234.368	-1118.886	1.62	0.28	high
11	02		CP	-2234.533	-1118.748	1.54	0.15	high
11	02		DO	-2234.413	-1118.811	1.48	0.26	high
11	02		DP	-2234.579	-1118.672	1.56	0.13	high
11	02		OP	-0.165	0.139	13.83	0.04	high
11	02		SC	-560.585	342.436	5.47	0.33	high
11	02		SD	-560.540	342.361	5.58	0.30	high
08	22		CD	0.010	-0.074	13.83	0.31	low
08	22		CO	-2792.305	-1303.980	1.08	0.21	low
08	22		CP	-2792.411	-1303.851	1.16	0.08	low
08	22		DO	-2792.316	-1303.906	1.17	0.17	low
08	22		DP	-2792.421	-1303.777	1.14	0.08	low
08	22		OP	-0.106	0.129	13.83	0.03	low
08	22		SC	-595.149	299.879	5.54	0.19	low
08	22		SD	-595.138	299.806	5.51	0.17	low
08	22		SO	-3387.454	-1004.100	0.59	0.12	low
08	22		SP	-3387.560	-1003.971	0.57	0.05	low
08	48		CD	0.017	-0.074	13.83	0.34	low
08	48		CP	-2791.781	-1271.778	1.12	0.08	low
08	48		DO	-2791.677	-1271.835	1.15	0.20	low
08	48		DP	-2791.797	-1271.705	1.12	0.08	low
08	48		OP	-0.120	0.130	13.83	0.03	low
08	48		SC	-609.874	306.800	5.55	0.20	low
08	48		SD	-609.857	306.727	5.55	0.20	low
08	48		SO	-3401.534	-965.108	0.73	0.11	low
08	48		SP	-3401.654	-964.978	0.75	0.05	low
09	14		CD	0.023	-0.074	13.83	0.36	low
09	14		CO	-2754.929	-1240.052	1.33	0.18	low
09	14		CP	-2755.061	-1239.921	1.22	0.09	low
09	14		DO	-2754.952	-1239.978	1.29	0.19	low
09	14		DP	-2755.085	-1239.847	1.19	0.09	low
09	14		OP	-0.133	0.132	13.83	0.03	low
09	14		SC	-616.715	313.845	5.30	0.20	low
09	14		SD	-616.692	313.771	5.40	0.20	low
09	14		SO	-3371.644	-926.207	0.66	0.11	low

Table 5 – continued

Day	hh	mm	Baseline	u (M λ)	v (M λ)	Flux Density (Jy)	σ (Jy)	Band
09	14		SP	-3371.777	-926.075	0.79	0.05	low
09	40		CD	0.029	-0.074	13.83	0.38	low
09	40		CO	-2682.585	-1208.822	1.43	0.19	low
09	40		CP	-2682.728	-1208.689	1.18	0.11	low
09	40		DO	-2682.614	-1208.748	1.14	0.20	low
09	40		DP	-2682.758	-1208.615	1.16	0.10	low
09	40		OP	-0.144	0.133	13.83	0.04	low
09	40		SC	-615.585	320.923	5.06	0.21	low
09	40		SD	-615.555	320.849	5.42	0.21	low
09	40		SO	-3298.170	-887.899	0.58	0.12	low
09	40		SP	-3298.313	-887.766	0.73	0.06	low
10	10		CD	0.036	-0.075	13.83	0.41	low
10	10		CO	-2556.104	-1174.093	1.31	0.26	low
10	10		CP	-2556.258	-1173.958	1.21	0.10	low
10	10		DO	-2556.140	-1174.018	1.07	0.22	low
10	10		DP	-2556.294	-1173.883	1.29	0.08	low
10	10		OP	-0.154	0.135	13.83	0.03	low
10	10		SC	-604.399	329.011	4.87	0.26	low
10	10		SD	-604.363	328.936	4.91	0.21	low
10	10		SO	-3160.502	-845.082	0.61	0.13	low
10	10		SP	-3160.656	-844.947	0.54	0.05	low
10	36		CD	0.041	-0.075	13.83	0.46	low
10	36		CO	-2410.818	-1145.566	1.34	0.25	low
10	36		CP	-2410.978	-1145.429	1.50	0.12	low
10	36		DO	-2410.859	-1145.490	1.37	0.20	low
10	36		DP	-2411.019	-1145.354	1.42	0.10	low
10	36		OP	-0.161	0.137	13.83	0.04	low
10	36		SC	-586.281	335.849	4.98	0.26	low
10	36		SD	-586.240	335.774	5.12	0.23	low
10	36		SO	-2997.099	-809.716	0.59	0.13	low
10	36		SP	-2997.260	-809.579	0.49	0.07	low
11	02		CD	0.046	-0.076	13.83	0.59	low
11	02		CO	-2234.368	-1118.886	1.65	0.28	low
11	02		CP	-2234.533	-1118.748	1.57	0.12	low
11	02		DO	-2234.413	-1118.811	1.51	0.25	low

Table 5 – continued

Day	hh	mm	Baseline	u (M λ)	v (M λ)	Flux Density (Jy)	σ (Jy)	Band
	11	02	DP	-2234.579	-1118.672	1.58	0.10	low
	11	02	OP	-0.165	0.139	13.83	0.03	low
	11	02	SC	-560.585	342.436	5.46	0.33	low
	11	02	SD	-560.540	342.361	5.59	0.29	low
	11	02	SP	-2795.119	-776.311	0.33	0.08	low
91	08	00	DO	-2771.483	-1326.100	1.25	0.15	high
	08	00	DP	-2771.578	-1325.972	1.32	0.11	high
	08	00	FD	-0.029	-0.047	13.83	0.11	high
	08	00	FO	-2771.512	-1326.147	1.25	0.08	high
	08	00	FP	-2771.607	-1326.019	1.24	0.07	high
	08	00	OP	-0.095	0.128	13.83	0.06	high
	08	00	SD	-580.364	295.117	5.15	0.10	high
	08	00	SF	-580.335	295.164	5.23	0.07	high
	08	00	SO	-3351.847	-1030.984	0.46	0.11	high
	08	00	SP	-3351.942	-1030.856	0.43	0.08	high
	08	27	DO	-2796.176	-1292.890	1.08	0.17	high
	08	27	DP	-2796.287	-1292.761	1.23	0.11	high
	08	27	FD	-0.023	-0.046	13.83	0.17	high
	08	27	FO	-2796.199	-1292.937	1.25	0.14	high
	08	27	FP	-2796.310	-1292.807	1.14	0.10	high
	08	27	OP	-0.111	0.129	13.83	0.06	high
	08	27	SD	-601.074	302.164	5.03	0.11	high
	08	27	SF	-601.050	302.210	5.01	0.10	high
	08	27	SO	-3397.250	-990.726	0.53	0.10	high
	08	27	SP	-3397.360	-990.597	0.52	0.07	high
	09	20	DO	-2731.482	-1227.952	1.28	0.16	high
	09	20	DP	-2731.619	-1227.820	1.14	0.11	high
	09	20	FD	-0.012	-0.046	13.83	0.12	high
	09	20	FO	-2731.495	-1227.998	1.23	0.09	high
	09	20	FP	-2731.632	-1227.866	1.19	0.06	high
	09	20	OP	-0.137	0.132	13.83	0.06	high
	09	20	SD	-617.200	316.476	4.79	0.11	high
	09	20	SF	-617.188	316.522	4.78	0.07	high
	09	20	SO	-3348.683	-911.476	0.53	0.10	high
	09	20	SP	-3348.820	-911.344	0.69	0.06	high

Table 5 – continued

Day	hh	mm	Baseline	u (M λ)	v (M λ)	Flux Density (Jy)	σ (Jy)	Band
	08	00	CD	0.006	-0.073	13.83	0.18	low
	08	00	CO	-2771.477	-1326.174	1.28	0.21	low
	08	00	CP	-2771.572	-1326.046	1.27	0.07	low
	08	00	DO	-2771.483	-1326.100	1.30	0.15	low
	08	00	DP	-2771.578	-1325.972	1.21	0.06	low
	08	00	OP	-0.095	0.128	13.83	0.04	low
	08	00	SC	-580.369	295.190	5.15	0.11	low
	08	00	SD	-580.364	295.117	5.15	0.10	low
	08	00	SP	-3351.942	-1030.856	0.40	0.04	low
	08	27	CD	0.013	-0.074	13.83	0.18	low
	08	27	CO	-2796.163	-1292.964	1.49	0.18	low
	08	27	CP	-2796.274	-1292.835	1.23	0.07	low
	08	27	DO	-2796.176	-1292.890	1.25	0.15	low
	08	27	DP	-2796.287	-1292.761	1.22	0.07	low
	08	27	OP	-0.111	0.129	13.83	0.04	low
	08	27	SC	-601.086	302.237	4.98	0.11	low
	08	27	SD	-601.074	302.164	5.00	0.10	low
	08	27	SO	-3397.250	-990.726	0.55	0.10	low
	08	27	SP	-3397.360	-990.597	0.61	0.04	low
	09	20	CD	0.026	-0.074	13.83	0.20	low
	09	20	CO	-2731.457	-1228.026	1.47	0.19	low
	09	20	CP	-2731.594	-1227.894	1.15	0.11	low
	09	20	DO	-2731.482	-1227.952	1.11	0.16	low
	09	20	DP	-2731.619	-1227.820	1.24	0.10	low
	09	20	OP	-0.137	0.132	13.83	0.05	low
	09	20	SC	-617.226	316.550	4.66	0.12	low
	09	20	SD	-617.200	316.476	4.69	0.10	low
	09	20	SO	-3348.683	-911.476	0.63	0.09	low
	09	20	SP	-3348.820	-911.344	0.65	0.05	low
92	08	00	DO	-2777.496	-1321.286	1.34	0.17	high
	08	00	DP	-2777.594	-1321.158	1.34	0.15	high
	08	00	FD	-0.028	-0.047	13.83	0.30	high
	08	00	FO	-2777.524	-1321.333	1.49	0.35	high
	08	00	OP	-0.097	0.128	13.83	0.09	high
	08	27	DO	-2796.522	-1288.038	1.19	0.19	high

Table 5 – continued

Day	hh	mm	Baseline	u (M λ)	v (M λ)	Flux Density (Jy)	σ (Jy)	Band
	08	27	FD	-0.023	-0.046	13.83	0.29	high
	08	27	OP	-0.113	0.129	13.83	0.09	high
	09	20	DO	-2720.763	-1223.222	1.37	0.15	high
	09	20	DP	-2720.902	-1223.089	1.37	0.11	high
	09	20	FD	-0.012	-0.046	13.83	0.29	high
	09	20	OP	-0.139	0.132	13.83	0.06	high
	09	20	SD	-617.080	317.547	5.11	0.14	high
	09	20	SF	-617.068	317.593	5.11	0.20	high
	09	20	SO	-3337.843	-905.675	0.65	0.12	high
	09	20	SP	-3337.982	-905.543	0.65	0.09	high
	08	00	OP	-0.097	0.128	13.83	0.06	low
	08	27	OP	-0.113	0.129	13.83	0.06	low
	09	20	CD	0.027	-0.074	13.83	0.26	low
	09	20	CO	-2720.737	-1223.296	1.40	0.23	low
	09	20	CP	-2720.876	-1223.163	1.30	0.11	low
	09	20	DO	-2720.763	-1223.222	1.32	0.14	low
	09	20	DP	-2720.902	-1223.089	1.29	0.07	low
	09	20	OP	-0.139	0.132	13.83	0.04	low
	09	20	SC	-617.106	317.621	5.08	0.20	low
	09	20	SD	-617.080	317.547	5.18	0.13	low
	09	20	SO	-3337.843	-905.675	0.59	0.13	low
	09	20	SP	-3337.982	-905.543	0.68	0.06	low
94	07	21	OP	-0.078	0.127	13.83	0.10	high
	07	21	SF	-551.282	288.362	5.67	0.06	high
	07	21	FO	-2707.567	-1359.077	1.64	0.07	high
	07	21	DO	-2707.533	-1359.030	1.61	0.17	high
	07	21	SD	-551.316	288.315	5.62	0.12	high
	07	21	DP	-2707.611	-1358.903	1.70	0.14	high
	07	21	FD	-0.033	-0.047	13.83	0.09	high
	07	21	FP	-2707.645	-1358.950	1.60	0.06	high
	07	47	SD	-579.249	294.809	4.90	0.12	high
	07	47	FO	-2769.505	-1327.620	1.45	0.10	high
	07	47	OP	-0.094	0.128	13.83	0.08	high
	07	47	SF	-579.220	294.855	5.06	0.08	high
	07	47	DO	-2769.477	-1327.573	1.57	0.16	high

Table 5 – continued

Day	hh	mm	Baseline	u (M λ)	v (M λ)	Flux Density (Jy)	σ (Jy)	Band
07	47		FD	-0.029	-0.047	13.83	0.12	high
07	47		DP	-2769.571	-1327.445	1.53	0.12	high
07	47		FP	-2769.600	-1327.492	1.47	0.08	high
07	47		SP	-3348.820	-1032.637	0.35	0.12	high
08	13		FP	-2795.753	-1295.528	1.43	0.08	high
08	13		DP	-2795.729	-1295.481	1.44	0.13	high
08	13		OP	-0.110	0.129	13.83	0.09	high
08	13		FD	-0.024	-0.046	13.83	0.11	high
08	13		SD	-599.694	301.580	4.72	0.12	high
08	13		SP	-3395.423	-993.902	0.56	0.11	high
08	13		SF	-599.670	301.626	4.79	0.07	high
08	13		FO	-2795.644	-1295.657	1.43	0.09	high
08	13		SO	-3395.313	-994.031	0.50	0.14	high
08	13		DO	-2795.620	-1295.610	1.50	0.16	high
08	39		FP	-2785.767	-1263.471	1.36	0.06	high
08	39		SO	-3398.012	-955.014	0.49	0.16	high
08	39		OP	-0.123	0.130	13.83	0.08	high
08	39		SP	-3398.135	-954.883	0.61	0.09	high
08	39		FD	-0.019	-0.046	13.83	0.11	high
08	39		SD	-612.387	308.541	4.91	0.13	high
08	39		DO	-2785.625	-1263.555	1.44	0.17	high
08	39		DP	-2785.748	-1263.424	1.37	0.11	high
08	39		SF	-612.368	308.587	4.97	0.07	high
08	39		FO	-2785.643	-1263.601	1.39	0.09	high
09	05		FO	-2739.634	-1231.867	1.38	0.11	high
09	05		SO	-3356.784	-916.218	0.56	0.14	high
09	05		DO	-2739.621	-1231.821	1.36	0.18	high
09	05		OP	-0.136	0.132	13.83	0.08	high
09	05		SP	-3356.920	-916.086	0.53	0.10	high
09	05		SF	-617.151	315.649	4.61	0.09	high
09	05		FD	-0.013	-0.046	13.83	0.15	high
09	05		DP	-2739.756	-1231.689	1.36	0.13	high
09	05		SD	-617.164	315.603	4.66	0.14	high
09	05		FP	-2739.770	-1231.735	1.40	0.09	high
09	31		FP	-2658.356	-1200.731	1.52	0.07	high

Table 5 – continued

Day	hh	mm	Baseline	u (M λ)	v (M λ)	Flux Density (Jy)	σ (Jy)	Band
09	31		DO	-2658.202	-1200.819	1.59	0.18	high
09	31		OP	-0.146	0.134	13.83	0.08	high
09	31		FD	-0.008	-0.046	13.83	0.12	high
09	31		SD	-613.963	322.674	4.61	0.15	high
09	31		FO	-2658.210	-1200.865	1.43	0.09	high
09	31		SO	-3272.165	-878.145	0.53	0.17	high
09	31		SP	-3272.311	-878.012	0.54	0.11	high
09	31		SF	-613.955	322.720	4.62	0.08	high
09	31		DP	-2658.349	-1200.686	1.40	0.13	high
09	57		FO	-2542.424	-1170.995	1.55	0.10	high
09	57		OP	-0.155	0.135	13.83	0.08	high
09	57		FD	-0.002	-0.046	13.83	0.15	high
09	57		DP	-2542.577	-1170.814	1.55	0.15	high
09	57		SD	-602.825	329.662	4.56	0.17	high
09	57		FP	-2542.579	-1170.860	1.55	0.08	high
09	57		SF	-602.823	329.708	4.55	0.09	high
09	57		DO	-2542.422	-1170.950	1.54	0.20	high
10	23		FP	-2393.935	-1142.508	1.88	0.10	high
10	23		OP	-0.161	0.137	13.83	0.08	high
10	23		DO	-2393.777	-1142.599	1.89	0.20	high
10	23		SF	-583.899	336.524	4.73	0.12	high
10	23		FO	-2393.773	-1142.645	1.84	0.12	high
10	23		DP	-2393.938	-1142.462	1.83	0.17	high
10	23		FD	0.004	-0.046	13.83	0.20	high
10	23		SD	-583.895	336.478	4.74	0.18	high
10	49		FO	-2214.179	-1116.179	1.81	0.12	high
10	49		FP	-2214.344	-1116.040	1.88	0.10	high
10	49		DO	-2214.188	-1116.133	1.91	0.22	high
10	49		FD	0.010	-0.046	13.83	0.22	high
10	49		OP	-0.166	0.139	13.83	0.08	high
10	49		DP	-2214.354	-1115.994	1.78	0.19	high
10	49		SD	-557.417	343.033	4.66	0.21	high
10	49		SF	-557.427	343.079	4.65	0.12	high
07	21		SC	-551.314	288.389	5.49	0.13	low
07	21		CD	-0.001	-0.073	13.83	0.20	low

Table 5 – continued

Day	hh	mm	Baseline	u (M λ)	v (M λ)	Flux Density (Jy)	σ (Jy)	Band
07	21		SD	-551.316	288.315	5.62	0.12	low
07	21		DP	-2707.611	-1358.903	1.54	0.09	low
07	21		DO	-2707.533	-1359.030	1.60	0.17	low
07	21		CO	-2707.535	-1359.103	1.94	0.24	low
07	21		OP	-0.078	0.127	13.83	0.07	low
07	21		CP	-2707.613	-1358.976	1.66	0.11	low
07	47		DP	-2769.571	-1327.445	1.56	0.08	low
07	47		SD	-579.249	294.809	4.90	0.12	low
07	47		CO	-2769.471	-1327.647	1.58	0.21	low
07	47		CD	0.005	-0.073	13.83	0.21	low
07	47		SC	-579.254	294.882	5.12	0.13	low
07	47		OP	-0.094	0.128	13.83	0.06	low
07	47		CP	-2769.566	-1327.519	1.49	0.09	low
07	47		DO	-2769.477	-1327.573	1.59	0.15	low
08	13		DO	-2795.620	-1295.610	1.52	0.17	low
08	13		CP	-2795.717	-1295.555	1.51	0.10	low
08	13		SD	-599.694	301.580	4.72	0.12	low
08	13		SP	-3395.423	-993.902	0.41	0.07	low
08	13		CO	-2795.608	-1295.684	1.53	0.23	low
08	13		OP	-0.110	0.129	13.83	0.06	low
08	13		DP	-2795.729	-1295.481	1.45	0.08	low
08	13		CD	0.012	-0.074	13.83	0.22	low
08	13		SC	-599.706	301.653	4.72	0.14	low
08	39		SD	-612.387	308.541	4.89	0.13	low
08	39		CO	-2785.606	-1263.629	1.70	0.21	low
08	39		SO	-3398.012	-955.014	0.51	0.14	low
08	39		SC	-612.405	308.615	4.76	0.14	low
08	39		DP	-2785.748	-1263.424	1.41	0.08	low
08	39		OP	-0.123	0.130	13.83	0.05	low
08	39		CP	-2785.730	-1263.498	1.46	0.09	low
08	39		DO	-2785.625	-1263.555	1.41	0.16	low
08	39		SP	-3398.135	-954.883	0.53	0.06	low
08	39		CD	0.019	-0.074	13.83	0.21	low
09	05		SO	-3356.784	-916.218	0.55	0.15	low
09	05		SC	-617.189	315.677	4.95	0.16	low

Table 5 – continued

Day	hh	mm	Baseline	u (M λ)	v (M λ)	Flux Density (Jy)	σ (Jy)	Band
09	05		SD	-617.164	315.603	4.67	0.14	low
09	05		OP	-0.136	0.132	13.83	0.05	low
09	05		DP	-2739.756	-1231.689	1.48	0.08	low
09	05		SP	-3356.920	-916.086	0.54	0.06	low
09	05		CD	0.025	-0.074	13.83	0.23	low
09	05		CO	-2739.596	-1231.895	1.56	0.24	low
09	05		DO	-2739.621	-1231.821	1.43	0.17	low
09	05		CP	-2739.731	-1231.763	1.33	0.10	low
09	31		DO	-2658.202	-1200.819	1.45	0.18	low
09	31		SC	-613.994	322.748	4.63	0.16	low
09	31		OP	-0.146	0.134	13.83	0.05	low
09	31		CO	-2658.172	-1200.893	1.79	0.23	low
09	31		SP	-3272.311	-878.012	0.50	0.06	low
09	31		DP	-2658.349	-1200.686	1.53	0.08	low
09	31		CD	0.031	-0.074	13.83	0.24	low
09	31		CP	-2658.318	-1200.760	1.47	0.10	low
09	31		SD	-613.963	322.674	4.61	0.14	low
09	57		DP	-2542.577	-1170.814	1.68	0.09	low
09	57		CO	-2542.386	-1171.024	1.89	0.24	low
09	57		SC	-602.862	329.737	4.58	0.17	low
09	57		SD	-602.825	329.662	4.56	0.16	low
09	57		OP	-0.155	0.135	13.83	0.05	low
09	57		SO	-3145.248	-841.287	0.53	0.14	low
09	57		CP	-2542.541	-1170.889	1.60	0.10	low
09	57		SP	-3145.402	-841.152	0.42	0.07	low
09	57		DO	-2542.422	-1170.950	1.47	0.20	low
09	57		CD	0.037	-0.075	13.83	0.28	low
10	23		OP	-0.161	0.137	13.83	0.06	low
10	23		DO	-2393.777	-1142.599	1.70	0.23	low
10	23		SC	-583.937	336.553	4.71	0.20	low
10	23		CD	0.042	-0.075	13.83	0.34	low
10	23		SD	-583.895	336.478	4.74	0.18	low
10	23		CO	-2393.736	-1142.674	1.90	0.28	low
10	23		DP	-2393.938	-1142.462	1.75	0.10	low
10	23		CP	-2393.897	-1142.537	1.73	0.12	low

Table 5 – continued

Day	hh	mm	Baseline	u (M λ)	v (M λ)	Flux Density (Jy)	σ (Jy)	Band
10	49		SC	-557.464	343.109	4.79	0.23	low
10	49		SD	-557.417	343.033	4.66	0.20	low
10	49		CD	0.046	-0.076	13.83	0.42	low
10	49		CO	-2214.142	-1116.209	2.22	0.31	low
10	49		DO	-2214.188	-1116.133	2.00	0.22	low
10	49		OP	-0.166	0.139	13.83	0.05	low
10	49		CP	-2214.308	-1116.070	1.95	0.13	low
10	49		DP	-2214.354	-1115.994	2.00	0.11	low

Table 6:: Closure phases of 3C 279

Day	hh	mm	Triangle	Closure Phase (Degree)	σ (Degree)	Band
88	08	34	CDP	-11.9	5.8	high
	09	32	CDP	-1.8	4.1	high
	08	34	CDJ	-0.3	5.6	high
	09	32	CDJ	-2.5	6.0	high
	10	01	CDJ	1.2	4.0	high
	08	34	CJP	-3.2	7.2	high
	09	32	CJP	2.7	4.7	high
	08	34	DJP	3.7	4.5	high
	09	32	DJP	1.1	4.1	high
	10	01	DJP	4.9	3.5	high
	07	26	SCD	-0.3	1.0	high
	08	34	SCD	-2.0	1.1	high
	09	32	SCD	-2.4	1.5	high
	10	01	SCD	2.6	1.1	high
	08	34	SJP	8.9	5.5	high
	09	32	SJP	0.1	6.0	high
	10	01	SJP	-3.2	4.2	high
	08	34	CDP	-4.6	4.9	low
	09	32	CDP	2.6	3.9	low
	10	01	CDP	-0.7	3.1	low
	08	34	CDJ	-10.1	3.8	low
	09	32	CDJ	-7.5	5.2	low

Table 6 – continued

Day	hh	mm	Triangle	Closure Phase (Degree)	σ (Degree)	Band
	10	01	CDJ	5.7	5.5	low
	08	34	CJP	1.6	3.6	low
	09	32	CJP	-1.7	4.9	low
	10	01	CJP	-6.2	4.8	low
	08	34	DJP	-8.5	5.2	low
	09	32	DJP	-8.9	4.8	low
	10	01	DJP	1.8	3.8	low
	07	26	SCD	-1.5	0.9	low
	08	34	SCD	-0.3	1.2	low
	09	32	SCD	-2.6	1.5	low
	08	34	SJP	2.8	4.7	low
	09	32	SJP	-2.0	4.5	low
	10	01	SJP	5.5	5.9	low
90	08	22	CDO	-8.0	6.8	high
	08	48	CDO	17.6	9.1	high
	09	14	CDO	-0.4	6.1	high
	09	40	CDO	9.4	5.4	high
	10	10	CDO	2.2	5.5	high
	10	36	CDO	-5.9	4.4	high
	11	02	CDO	-5.3	4.6	high
	08	22	CDP	-0.4	3.3	high
	08	48	CDP	-3.9	3.9	high
	09	14	CDP	3.3	3.7	high
	09	40	CDP	-4.2	3.2	high
	10	10	CDP	0.6	3.8	high
	10	36	CDP	-4.5	2.9	high
	11	02	CDP	-0.9	3.9	high
	08	22	COP	1.6	4.4	high
	08	48	COP	1.5	5.0	high
	09	14	COP	-1.1	5.5	high
	09	40	COP	-1.6	4.1	high
	10	10	COP	-5.2	4.8	high
	10	36	COP	-2.9	3.9	high
	11	02	COP	2.9	6.2	high
	08	22	DOP	-9.4	4.7	high

Table 6 – continued

Day	hh	mm	Triangle	Closure Phase (Degree)	σ (Degree)	Band
08	48		DOP	15.8	4.2	high
09	14		DOP	-7.0	3.6	high
09	40		DOP	12.0	4.2	high
10	10		DOP	-1.0	4.6	high
10	36		DOP	-0.5	4.7	high
11	02		DOP	-3.3	4.5	high
08	22		SCD	-1.5	1.2	high
08	48		SCD	0.4	2.6	high
09	14		SCD	1.3	1.6	high
09	40		SCD	-3.8	2.1	high
10	10		SCD	0.4	2.3	high
10	36		SCD	-3.3	2.9	high
11	02		SCD	0.6	1.9	high
08	22		SOP	-1.8	6.8	high
08	48		SOP	-7.5	5.9	high
09	14		SOP	4.6	4.9	high
09	40		SOP	6.1	5.2	high
10	10		SOP	5.3	6.0	high
08	22		CDO	-3.2	6.4	low
09	14		CDO	5.3	6.3	low
09	40		CDO	3.6	4.4	low
10	10		CDO	-0.2	6.9	low
10	36		CDO	3.4	6.3	low
11	02		CDO	-2.6	6.1	low
08	22		CDP	-1.0	2.6	low
08	48		CDP	-1.6	3.6	low
09	14		CDP	-0.7	2.5	low
09	40		CDP	5.6	4.0	low
10	10		CDP	-1.1	3.0	low
10	36		CDP	-0.6	3.3	low
11	02		CDP	-4.1	3.2	low
08	22		DOP	0.0	2.9	low
08	48		DOP	-3.0	5.9	low
09	14		DOP	2.1	4.7	low
09	40		DOP	1.7	4.1	low

Table 6 – continued

Day	hh	mm	Triangle	Closure Phase (Degree)	σ (Degree)	Band
	10	10	DOP	9.1	4.7	low
	10	36	DOP	0.7	4.4	low
	11	02	DOP	1.7	5.4	low
	08	22	SCD	-3.3	1.3	low
	08	48	SCD	-1.8	1.8	low
	09	14	SCD	1.9	2.3	low
	09	40	SCD	1.4	2.2	low
	10	10	SCD	-1.7	1.9	low
	10	36	SCD	0.3	2.7	low
	11	02	SCD	-4.4	3.0	low
	08	22	COP	-3.0	6.1	low
	09	14	COP	0.6	5.0	low
	09	40	COP	2.7	4.7	low
	10	10	COP	4.4	4.6	low
	10	36	COP	-1.7	5.5	low
	11	02	COP	-4.2	4.0	low
	08	22	SOP	2.4	4.0	low
	08	48	SOP	-2.7	4.7	low
	09	14	SOP	-1.9	3.4	low
	09	40	SOP	3.6	3.7	low
	10	10	SOP	-10.7	5.4	low
	10	36	SOP	-5.6	14.2	low
91	08	00	SFD	-1.9	0.7	high
	08	27	SFD	-0.4	1.0	high
	09	20	SFD	-1.5	1.3	high
	08	00	FDO	-4.6	4.2	high
	08	27	FDO	-4.8	5.4	high
	09	20	FDO	-5.3	3.3	high
	08	00	DOP	-5.3	4.8	high
	08	27	DOP	-5.1	4.1	high
	09	20	DOP	-3.1	2.9	high
	08	00	FDP	3.7	2.4	high
	08	27	FDP	4.8	4.0	high
	09	20	FDP	1.6	3.2	high
	08	00	FOP	2.7	2.2	high

Table 6 – continued

Day	hh	mm	Triangle	Closure Phase (Degree)	σ (Degree)	Band
	08	27	FOP	7.4	4.3	high
	09	20	FOP	2.8	2.7	high
	08	00	SOP	-9.9	6.5	high
	08	27	SOP	4.9	6.0	high
	09	20	SOP	4.7	4.8	high
	08	00	CDO	11.6	5.1	low
	08	27	CDO	7.0	4.3	low
	09	20	CDO	-6.2	3.7	low
	08	00	CDP	-2.2	2.9	low
	08	27	CDP	0.0	2.5	low
	09	20	CDP	5.9	3.3	low
	08	00	COP	-2.1	4.4	low
	08	27	COP	-5.0	4.4	low
	09	20	COP	8.5	4.2	low
	08	00	DOP	12.1	4.7	low
	08	27	DOP	2.3	4.3	low
	09	20	DOP	4.1	3.5	low
	08	00	SCD	-1.0	1.0	low
	08	27	SCD	-0.6	1.3	low
	09	20	SCD	-0.9	1.3	low
	08	27	SOP	-0.5	3.7	low
	09	20	SOP	1.6	3.6	low
92	08	00	FDO	1.5	8.8	high
	08	00	SFD	-4.3	1.6	high
	08	27	SFD	2.0	2.9	high
	09	20	SFD	2.8	2.8	high
	08	00	DOP	-1.1	4.2	high
	09	20	DOP	5.2	4.5	high
	08	27	SOP	-3.2	6.5	high
	09	20	SOP	-0.6	5.1	high
	09	20	CDO	6.7	6.2	low
	08	00	DOP	2.4	4.4	low
	08	27	DOP	0.3	6.9	low
	09	20	DOP	5.6	4.9	low
	09	20	CDP	-3.6	4.5	low

Table 6 – continued

Day	hh	mm	Triangle	Closure Phase (Degree)	σ (Degree)	Band
	09	20	COP	-2.0	7.5	low
	09	20	SCD	0.0	2.5	low
	08	00	SOP	4.6	5.5	low
	08	27	SOP	6.9	6.5	low
	09	20	SOP	3.7	5.0	low
94	07	21	FDP	1.5	2.5	high
	07	47	FDP	1.0	2.7	high
	08	13	FDP	-1.4	3.1	high
	08	39	FDP	-3.4	2.9	high
	09	05	FDP	1.1	4.9	high
	09	31	FDP	1.7	3.4	high
	09	57	FDP	0.6	3.5	high
	10	23	FDP	0.5	3.4	high
	10	49	FDP	0.2	3.0	high
	07	21	FDO	-4.3	3.2	high
	07	47	FDO	-0.3	4.8	high
	08	13	FDO	-4.1	2.6	high
	08	39	FDO	-0.9	3.5	high
	09	05	FDO	-3.4	5.3	high
	09	31	FDO	-2.2	2.8	high
	09	57	FDO	2.7	3.1	high
	10	23	FDO	3.1	4.0	high
	10	49	FDO	6.5	3.4	high
	07	21	FOP	1.3	1.8	high
	07	47	FOP	-0.3	2.6	high
	08	13	FOP	0.0	2.1	high
	08	39	FOP	-2.4	2.1	high
	09	05	FOP	-0.1	2.5	high
	09	31	FOP	1.7	2.3	high
	09	57	FOP	-1.5	1.7	high
	10	23	FOP	-6.7	2.5	high
	10	49	FOP	-2.5	2.2	high
	07	21	DOP	-3.6	2.5	high
	07	47	DOP	-1.8	4.0	high
	08	13	DOP	2.2	4.5	high

Table 6 – continued

Day	hh	mm	Triangle	Closure Phase (Degree)	σ (Degree)	Band
08	39		DOP	-0.3	3.9	high
09	05		DOP	-3.0	5.7	high
09	31		DOP	-3.1	4.3	high
09	57		DOP	-2.3	4.7	high
10	23		DOP	-4.7	3.5	high
10	49		DOP	4.1	5.2	high
07	21		SFD	-0.4	0.8	high
07	47		SFD	0.5	1.1	high
08	13		SFD	-1.3	1.2	high
08	39		SFD	0.6	0.8	high
09	05		SFD	3.4	1.4	high
09	31		SFD	0.5	1.2	high
09	57		SFD	-0.1	1.4	high
10	23		SFD	-2.7	1.6	high
10	49		SFD	-1.4	1.4	high
08	13		SOP	1.3	7.1	high
08	39		SOP	11.7	8.6	high
09	05		SOP	2.7	11.7	high
09	31		SOP	0.2	8.5	high
09	57		SOP	-7.2	8.8	high
07	21		CDO	-3.9	4.1	low
07	47		CDO	4.5	5.0	low
08	13		CDO	-1.1	6.6	low
08	39		CDO	0.8	6.0	low
09	05		CDO	-4.7	5.7	low
09	31		CDO	1.3	5.6	low
09	57		CDO	-1.2	4.9	low
10	49		CDO	4.8	5.0	low
07	21		CDP	4.1	2.7	low
07	47		CDP	0.2	2.3	low
08	13		CDP	-3.1	2.8	low
08	39		CDP	7.6	2.6	low
09	05		CDP	1.1	2.6	low
09	31		CDP	0.3	2.7	low
09	57		CDP	-2.8	2.9	low

Table 6 – continued

Day	hh	mm	Triangle	Closure Phase (Degree)	σ (Degree)	Band
	10	23	CDP	2.7	3.3	low
	10	49	CDP	-0.3	2.5	low
	07	21	COP	0.0	2.7	low
	07	47	COP	-4.0	3.6	low
	08	13	COP	0.1	3.8	low
	08	39	COP	6.5	4.5	low
	09	05	COP	-0.2	4.9	low
	09	31	COP	-2.2	3.2	low
	09	57	COP	1.3	4.2	low
	10	23	COP	-3.5	3.5	low
	10	49	COP	-6.6	4.2	low
	07	21	DOP	-4.6	4.3	low
	07	47	DOP	-4.0	3.1	low
	08	13	DOP	-3.4	4.5	low
	08	39	DOP	0.1	3.8	low
	09	05	DOP	-6.4	3.1	low
	09	31	DOP	-4.3	3.5	low
	09	57	DOP	3.5	3.4	low
	10	23	DOP	2.2	4.1	low
	10	49	DOP	-1.0	4.0	low
	07	21	SCD	-2.2	1.2	low
	07	47	SCD	-4.1	1.5	low
	08	13	SCD	-3.6	1.3	low
	08	39	SCD	-0.6	1.7	low
	09	05	SCD	-4.4	1.7	low
	09	31	SCD	-4.1	1.7	low
	09	57	SCD	0.0	1.9	low
	10	23	SCD	-0.3	1.9	low
	10	49	SCD	2.1	2.4	low
	07	21	SOP	10.8	16.0	low
	09	05	SOP	-6.0	6.0	low
	09	31	SOP	-8.5	9.8	low
88	08	34	SCP	-126.2	6.3	high
	09	32	SCP	-136.5	5.1	high
	08	34	SDP	-137.6	4.9	high

Table 6 – continued

Day	hh	mm	Triangle	Closure Phase (Degree)	σ (Degree)	Band
	09	32	SDP	-135.1	4.2	high
	10	01	SDP	-146.6	4.4	high
	08	34	SCJ	-138.8	7.8	high
	09	32	SCJ	-135.1	5.6	high
	10	01	SCJ	-137.8	6.3	high
	08	34	SDJ	-142.9	6.4	high
	09	32	SDJ	-133.3	6.5	high
	10	01	SDJ	-138.0	6.0	high
	08	34	SCP	-124.0	4.5	low
	09	32	SCP	-140.6	3.1	low
	10	01	SCP	-135.2	4.3	low
	08	34	SDP	-129.7	5.2	low
	09	32	SDP	-134.3	3.7	low
	08	34	SCJ	-126.9	4.6	low
	09	32	SCJ	-140.0	5.1	low
	10	01	SCJ	-145.5	5.7	low
	08	34	SDJ	-140.7	6.3	low
	09	32	SDJ	-143.5	4.2	low
90	08	22	SCO	-130.1	8.2	high
	08	48	SCO	-129.4	6.9	high
	09	14	SCO	-143.5	5.5	high
	09	40	SCO	-150.1	3.9	high
	10	10	SCO	-135.6	6.2	high
	08	22	SDO	-139.3	10.3	high
	08	48	SDO	-119.1	5.3	high
	09	14	SDO	-149.9	4.5	high
	09	40	SDO	-133.8	5.8	high
	10	10	SDO	-141.2	4.7	high
	08	22	SCP	-130.0	3.3	high
	08	48	SCP	-138.0	4.2	high
	09	14	SCP	-137.1	3.3	high
	09	40	SCP	-137.2	3.5	high
	10	10	SCP	-126.1	5.8	high
	10	36	SCP	-110.3	5.2	high
	11	02	SCP	-91.2	6.1	high

Table 6 – continued

Day	hh	mm	Triangle	Closure Phase (Degree)	σ (Degree)	Band
	08	22	SDP	-127.1	3.2	high
	08	48	SDP	-139.3	4.0	high
	09	14	SDP	-135.9	4.4	high
	09	40	SDP	-138.4	3.9	high
	10	10	SDP	-127.8	5.7	high
	10	36	SDP	-116.1	5.3	high
	11	02	SDP	-96.1	4.7	high
	08	22	SDO	-127.9	5.7	low
	08	48	SDO	-135.9	5.1	low
	09	14	SDO	-136.4	4.9	low
	09	40	SDO	-137.9	3.6	low
	10	10	SDO	-116.9	5.8	low
	10	36	SDO	-108.0	13.0	low
	08	22	SDP	-127.7	3.0	low
	08	48	SDP	-138.0	2.6	low
	09	14	SDP	-139.7	2.2	low
	09	40	SDP	-134.1	3.1	low
	10	10	SDP	-135.7	3.3	low
	10	36	SDP	-128.0	3.5	low
	11	02	SDP	-86.5	5.8	low
	08	22	SCO	-135.5	8.3	low
	09	14	SCO	-135.1	5.2	low
	09	40	SCO	-138.5	4.4	low
	10	10	SCO	-121.9	7.4	low
	10	36	SCO	-111.3	10.0	low
	08	22	SCP	-129.5	3.6	low
	08	48	SCP	-137.7	3.1	low
	09	14	SCP	-139.1	2.4	low
	09	40	SCP	-138.5	4.1	low
	10	10	SCP	-136.9	4.2	low
	10	36	SCP	-126.1	4.6	low
	11	02	SCP	-88.1	5.4	low
91	08	00	SDO	-131.2	6.4	high
	08	27	SDO	-137.8	4.9	high
	09	20	SDO	-148.8	4.6	high

Table 6 – continued

Day	hh	mm	Triangle	Closure Phase (Degree)	σ (Degree)	Band
	08	00	SDP	-145.0	4.1	high
	08	27	SDP	-130.9	4.0	high
	09	20	SDP	-137.9	3.1	high
	08	00	SFO	-130.6	5.1	high
	08	27	SFO	-134.2	4.5	high
	09	20	SFO	-142.0	4.9	high
	08	00	SFP	-147.4	4.7	high
	08	27	SFP	-135.5	3.7	high
	09	20	SFP	-141.7	2.7	high
	08	27	SCO	-141.4	5.0	low
	09	20	SCO	-138.5	4.4	low
	08	00	SCP	-127.7	3.4	low
	08	27	SCP	-135.4	2.1	low
	09	20	SCP	-146.3	4.1	low
	08	27	SDO	-133.7	4.8	low
	09	20	SDO	-138.8	4.1	low
	08	00	SDP	-128.4	3.1	low
	08	27	SDP	-134.6	2.6	low
	09	20	SDP	-138.1	2.5	low
92	08	27	SDO	-136.4	8.0	high
	09	20	SDO	-152.4	8.8	high
	08	00	SDP	-136.3	5.8	high
	09	20	SDP	-155.5	5.2	high
	08	00	SDO	-134.6	6.1	low
	08	27	SDO	-154.1	7.6	low
	09	20	SDO	-147.0	7.6	low
	08	00	SDP	-133.4	4.1	low
	08	27	SDP	-143.6	4.6	low
	09	20	SDP	-151.0	3.6	low
	09	20	SCO	-142.5	8.3	low
	09	20	SCP	-146.4	4.3	low
94	08	13	SFP	-160.7	4.8	high
	08	39	SFP	-154.7	4.3	high
	09	05	SFP	-160.9	5.3	high
	09	31	SFP	-159.0	5.3	high

Table 6 – continued

Day	hh	mm	Triangle	Closure Phase (Degree)	σ (Degree)	Band
09	57		SFP	-147.5	5.1	high
08	13		SDO	-155.2	8.1	high
08	39		SDO	-174.4	6.4	high
09	05		SDO	-167.3	8.4	high
09	31		SDO	-158.0	7.7	high
09	57		SDO	-146.3	7.3	high
08	13		SFO	-153.7	8.2	high
08	39		SFO	-167.9	5.4	high
09	05		SFO	-159.9	5.8	high
09	31		SFO	-150.5	6.9	high
09	57		SFO	-142.4	9.0	high
08	13		SDP	-160.5	5.2	high
08	39		SDP	-157.7	5.7	high
09	05		SDP	-169.1	5.1	high
09	31		SDP	-160.6	6.3	high
09	57		SDP	-149.9	6.5	high
08	13		SCO	-153.9	12.2	low
09	05		SCO	-157.0	8.7	low
09	31		SCO	-149.8	10.2	low
08	13		SDO	-161.6	13.5	low
09	05		SDO	-156.6	5.7	low
09	31		SDO	-140.2	11.2	low
07	21		SCP	-135.1	30.8	low
07	47		SCP	-136.9	7.1	low
08	13		SCP	-145.0	4.8	low
08	39		SCP	-159.3	3.9	low
09	05		SCP	-160.6	3.5	low
09	31		SCP	-155.7	3.2	low
09	57		SCP	-145.3	3.8	low
10	49		SCP	-43.2	7.5	low
07	21		SDP	-133.2	26.6	low
07	47		SDP	-136.0	7.0	low
08	13		SDP	-143.6	5.0	low
08	39		SDP	-151.6	4.1	low
09	05		SDP	-155.9	3.1	low

Table 6 – continued

Day	hh	mm	Triangle	Closure Phase (Degree)	σ (Degree)	Band
	09	31	SDP	-150.1	3.4	low
	09	57	SDP	-149.0	3.9	low
	10	49	SDP	-39.7	7.6	low